ASSESSING THE EFFECT OF COUPLED GEOMECHANICAL AND FLUID-FLOW PROBLEMS IN GEOTHERMAL RESERVOIRS VIA NUMERICAL MODELING

A THESIS SUBMITTED TO THE GRADUATE SCHOOL OF NATURAL AND APPLIED SCIENCES OF
MIDDLE EAST TECHNICAL UNIVESITY (METU)

BY

YUSSIF MUSTAPHA

IN PARTIAL FULFILLMENT OF THE REQUIREMENTS
FOR
THE DEGREE OF MASTER OF SCIENCE
IN
PETROLEUM AND NATURAL GAS ENGINEERING

SEPTEMBER, 2024

Approval of the thesis:

ASSESSING THE EFFECT OF COUPLED GEOMECHANICAL AND FLUID-FLOW PROBLEMS IN GEOTHERMAL RESERVOIRS VIA NUMERICAL MODELING

submitted by **YUSSIF MUSTAPHA** in partial fulfillment of the requirements for the degree of **Master of Science** i**n Petroleum and Natural Gas Engineering, Middle East Technical University** by,

Prof. Dr. Naci Emre Altun
Dean, **Graduate School of Natural and Applied Sciences** _____

Assoc. Prof. Dr. İsmail Durgut
Head of the Department, **Petroleum and Natural Gas Eng.** _____

Assist. Prof. Dr. Mehmet Onur Doğan
Supervisor, **Petroleum and Natural Gas Eng., METU** _____

Examining Committee Members:

Assist. Prof. Dr. Betül Yıldırım
Petroleum and Natural Gas Eng, METU _____

Assist. Prof. Dr. Mehmet Onur Doğan
Petroleum and Natural Gas Eng, METU _____

Assist. Prof. Dr. Selçuk Erol
Energy System Engineering, IZTECH _____

Date: 05.09.2024

I hereby declare that all information in this document has been obtained and presented in accordance with academic rules and ethical conduct. I also declare that, as required by these rules and conduct, I have fully cited and referenced all material and results that are not original to this work.

Name Last name: Yussif Mustapha
Signature:

ABSTRACT

ASSESSING THE EFFECT OF COUPLED GEOMECHANICAL AND FLUID-FLOW PROBLEMS IN GEOTHERMAL RESERVOIRS VIA NUMERICAL MODELING

Yussif Mustapha
Master of Science, Petroleum and Natural Gas Engineering
Supervisor: Assist. Prof. Dr. Mehmet Onur Doğan

September 2024, 84 pages

Until recently, reservoir simulations were conducted in the stand-alone way; this conventional method assumed porosity and permeability are independent of the stresses in the porous media. Recent studies have found out that overlooking geomechanical effects during reservoir simulation leads to inaccurate estimations of pressure and volume. It is therefore necessary to couple the geomechanical and fluid flow effects for a more accurate representation of reality.
Coupled geomechanical and fluid flow problems can be encountered in many reservoir operations, e.g., EOR, CO2 sequestration, and geothermal reservoirs. In order to enhance oil recovery processes, external fluids such as water or CO2 can be injected into the reservoir. The injected fluid might not only change the oil properties, e.g., viscosity, but also reservoir rock properties, i.e., porosity and permeability, via increased reservoir pressure. Pressure changes lead to the expansion or contraction of the reservoir, which eventually alters the stress and strain distribution in the reservoir. At the same time, the changes in the pore space affect the fluid flow equations. This coupled problem can be represented by poroelasticity models. In geothermal reservoirs, thermal stresses can be dominant. In this case, thermo-poroelastic models should be used to accurately model the long-term behavior of the geothermal reservoir. In this thesis, such kinds of coupled thermal, geomechanical, and fluid flow conservation equations will be explored and the essential coupling terms will be presented. The effect of thermo-poroelasticity will be shown on a fractured geothermal reservoir for a short-circuiting fracture flow problem.

Keywords: coupled problems, thermo-poroelasticity, short-circuiting

ÖZ

JEOTERMAL REZERVUARLARDAKİ BAĞLANTILI JEOMEKANİK VE AKIŞKAN AKIŞ SORUNLARININ SAYISAL MODELLEME İLE ETKİSİNİN DEĞERLENDİRİLMESİ

Mustapha, Yussif
Yüksek Lisans, Petrol ve Doğal gaz Mühendisliği
Tez Yöneticisi: Assist. Prof. Dr. Mehmet Onur Doğan

Eylül 2024, 84 sayfa

Yakın zamana kadar, rezervuar simülasyonları bağımsız bir şekilde yürütülüyordu; bu geleneksel yöntem, gözeneklilik ve geçirgenliğin gözenekli ortamdaki gerilimlerden bağımsız olduğunu varsaymıştır. Son çalışmalar, rezervuar simülasyonu sırasında jeomekanik etkilerin göz ardı edilmesinin, yanlış basınç ve hacim tahminlerine yol açtığını bulmuştur.
Birçok rezervuar operasyonunda, örneğin EOR, CO2 sekestrasyonu ve jeotermal rezervuarlar gibi, birleşik jeomekanik ve akış problemleriyle karşılaşılabilir. Petrol geri kazanım süreçlerini iyileştirmek için su veya CO2 gibi akışkanlar rezervuara enjekte edilebilir. Enjekte edilen akışkan, sadece petrolün viskozite gibi özelliklerini değil, aynı zamanda rezervuar kayaç özelliklerini, yani gözeneklilik ve geçirgenlik gibi özelliklerini de artırılmış rezervuar basıncı yoluyla değiştirebilir. Basınç değişiklikleri, rezervuarın genişlemesine veya büzülmesine yol açarak, rezervuardaki gerilme ve deformasyon dağılımını değiştirir. Aynı zamanda, gözenekli alandaki değişiklikler akış denklemlerini etkiler. Bu akuple problem, poroelastisite modeller ile çözülebilir. Jeotermal rezervuarlarda termal gerilmeler baskın olabilir. Bu durumda, jeotermal rezervuarın uzun süreli davranışını doğru bir şekilde modellemek için termo poroelastik modeller kullanılmalıdır. Bu tezde, bu tür birleşik termal, jeomekanik ve akışkan akışı koruma denklemleri sayısal olarak birlikte çözülecektir. Termo poroelastisitenin etkisi, kısa devre yapan bir çatlak akışı problemi için çatlaklı bir jeotermal rezervuar üzerinde gösterilecektir.

Anahtar Kelimeler: birleşik problemler, termo poroelastisite, kısa devre

I wholeheartedly dedicate this piece of work, first, to my caring mother, Raiya Ali, and then to my wife, Sahadatu Aminu, without whose love, care and support I would not be in such magnificent spirits as to successfully embark on this academic journey.

ACKNOWLEDGMENTS

The author wishes to express his sincerest gratitude to his supervisor Prof. Dr. Mehmet Onur Doğan for his unconditional guidance, advice, criticism, encouragements and insight throughout the research.
The author would also like to thank Assoc. Prof. Dr. Betül Yıldırım for her suggestions and comments.
The impactful knowledge and skills of Dr. B. Sadık Bakır and Assist. Prof. Dr. Selçuk Erol are gratefully acknowledged.
This work is wholly funded by Türkiye Bursları Scholarship program of the Turkish Government.

The ultimate Glory, notwithstanding, be to the Almighty Maker.

TABLE OF CONTENTS

LIST OF TABLES

TABLES

LIST OF FIGURES

FIGURES

CHAPTER 1

INTRODUCTION

According to the Intergovernmental Plan on Climate Change (IPCC)'s 2023 report, the energy sector is responsible for 34 percent of Greenhouse Gas (GHG) emissions caused by humans. The reality still holds that our energy sector, even in an era of booming EV's industry [as at 2023 EV's accounted for up to15% of the global car sales and are expected to reach 40% by 2030, see (International Energy Agency (IEA), 2023)] and a continuous rise in solar and wind energy, is yet dominated by fossil fuels. The global energy sector is currently releasing a whopping 20 Gigatons of GHG. This amount must be halved by 2030 in order to meet the goals in Paris Agreement.

Geothermal energy (excess steam or heat extracted from the earth's subsurface) today is used in heating, cooling and generation of electricity. Geothermal heat is considered as clean energy since no gases or liquids are released during the process, making it an essential instrument in the world's quest of zero-Carbon future. Furthermore, geothermal plants are operated at a relatively lower cost compared with other sources (cost of electricity from geothermal energy plateaued at $0.085/KWh at the end of 2020 and make up a significant fraction of the energy demands in countries such as the Philippines, Kenya, El Salvador and New Zealand, while covering 90% of demands in Iceland [see (IRENA and CPI, 2023)].

Today, the geothermal energy production is seeing a boom, thanks to Enhanced Geothermal Systems (EGS), in other words human-made geothermal energy. An EGS is formed when fluid (mainly water) is injected at high pressures into extremely low-permeability geothermal reservoir in order to create new fractures and reinforce existing fractures, making it possible to produce energy from an otherwise conventionally non-productive system.

In recent years, numerical simulation of subsurface systems has been revolutionized with coupled poroelasticity or, in a more comprehensive case, thermo-poroelasticity, in which the thermal effects are coupled with geomechanics and fluid flow processes. Works by (Aktan & Ali, 1978), (Pao et al., 2001), (McLean & Espinoza, 2023), etc. have proven the essence of coupling these effects as they have helped understand the causes and effects of hitherto puzzling phenomena such as porosity and permeability changes (which have direct effect on more economical parameters such as production rate, productivity index (PI), Stock tank oil in place (STOIP), as well as geomechanical responses such as thermal stress and short-circuiting, to name a few. Some prevailing methods of solving the equations involved include the finite element method (FEM) and volume method (FVM), which are used to discretize the

domain spatially, while the Euler scheme is effective in discretizing the domain temporally using the backward difference approximation [see (Beck, 2019)].
It is important to note that the models presented in this work are assumed to remain within elastic deformation at all time. In other words, analyses of the material's failure criterion will not be necessary since the yield point will not be exceeded, and therefore, no new fractures will form within the porous medium. Moreover, any EGS model presented comes with an existing human-made fractures by definition. The paramount contribution of this thesis shall be an experimental coupling of poroelastic model with thermal stresses and parametric analyses of several thermo-poroelastic properties, including the effect of fracture deformation on fracture permeability.

CHAPTER 2

LITERATURE REVIEW

Austrian mechanical, geotechnical engineer and geologist Karl von Terzaghi (1883-1963) and Belgian-America applied physicist Maurice Anthony Biot (1905-1985) are generally regarded as the pioneers of poroelasticity (i.e. the process of fluid flow in a deforming porous media). The former's well-known one-dimensional consolidation theory (later expanded to three-dimensional himself and several other authors) is still applied in geotechnical lab experiments, while the latter's three-dimensional consolidation theory, developed in a series of papers (Maurice A. Biot, 1941, 1955, 1956), are applied in various fields such and petroleum and geotechnical engineering as well as medical sciences and continuum biomechanics (Teichtmeister et al., 2019). One distinctive difference between Terzaghi's theory and Biot's theory is that while Terzaghi's solution show a continuous pressure depletion, Biot's reveal a non-monotonic pressure decrease – meaning, there is an initial pressure rise even as drainage continues before pressure starts to decrease.

2.1 Mandel-Cryer Effect

In 1953, (Mandel, J., 1953) set out to develop one of the earliest solutions to Biot's theory of three-dimensional consolidation. His model involved an infinitely long rectangular specimen sandwiched above and below by two rigid, frictionless plates. The model's lateral sides are free from normal stresses, shear stresses and pore pressure, allowing drainage across both sides, as shown on Figure 2-1. A uniform load is applied to the rigid plates at $t = 0^+$, creating a uniform pore pressure, which dissipates in time as drainage continues via the lateral sides of the specimen.

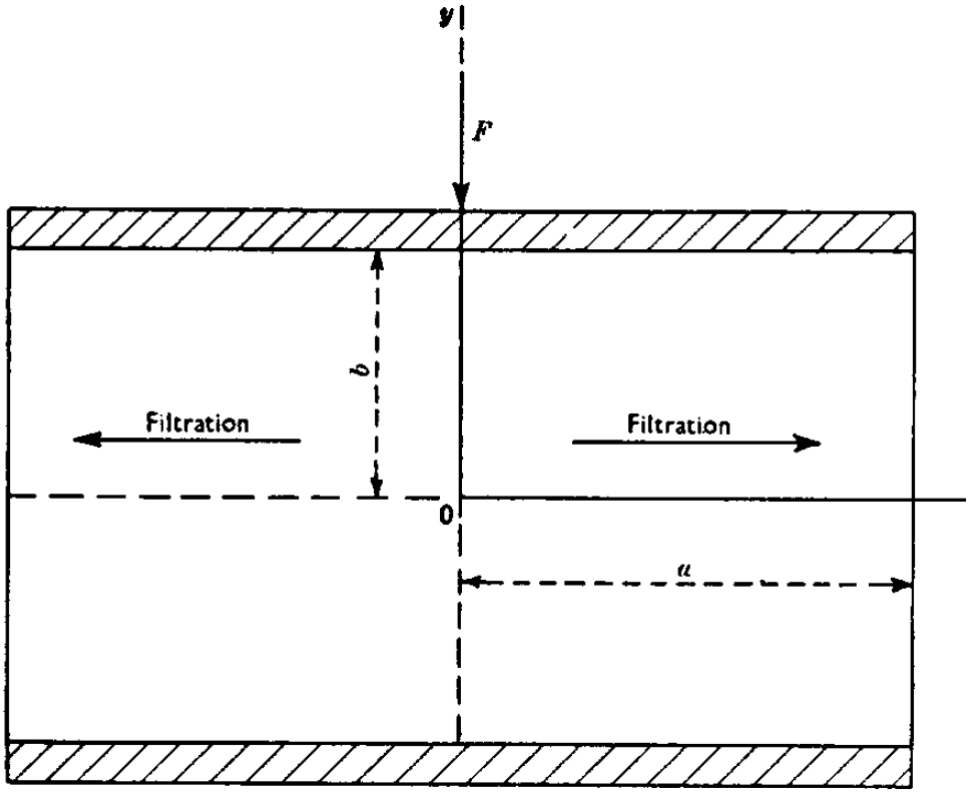

Figure 2-1. Set-up of Mandel's problem.

The generated pore pressure adds to the apparent compressive stiffness of the material, and therefore the specimen becomes more compliant near the lateral sides due to drainage. As required by compatibility, a load transfer of compressive total stress occurs towards the relatively stiffer center, which works as a pore pressure generation mechanism, thereby causing an increase in pore pressure at the centre region even as drainage (pressure depletion) continues across the lateral sides (Abousleiman et al., 1996).

After Mandel, another significant study of Biot's 3-D consolidation theory was made by South African Applied Mathematician Colin Walker Cryer in 1963. Just as Mandel, he observed the non-monotonic pressure response in the center of a spherical pack of soil subject to uniform load (Cryer, 1963).

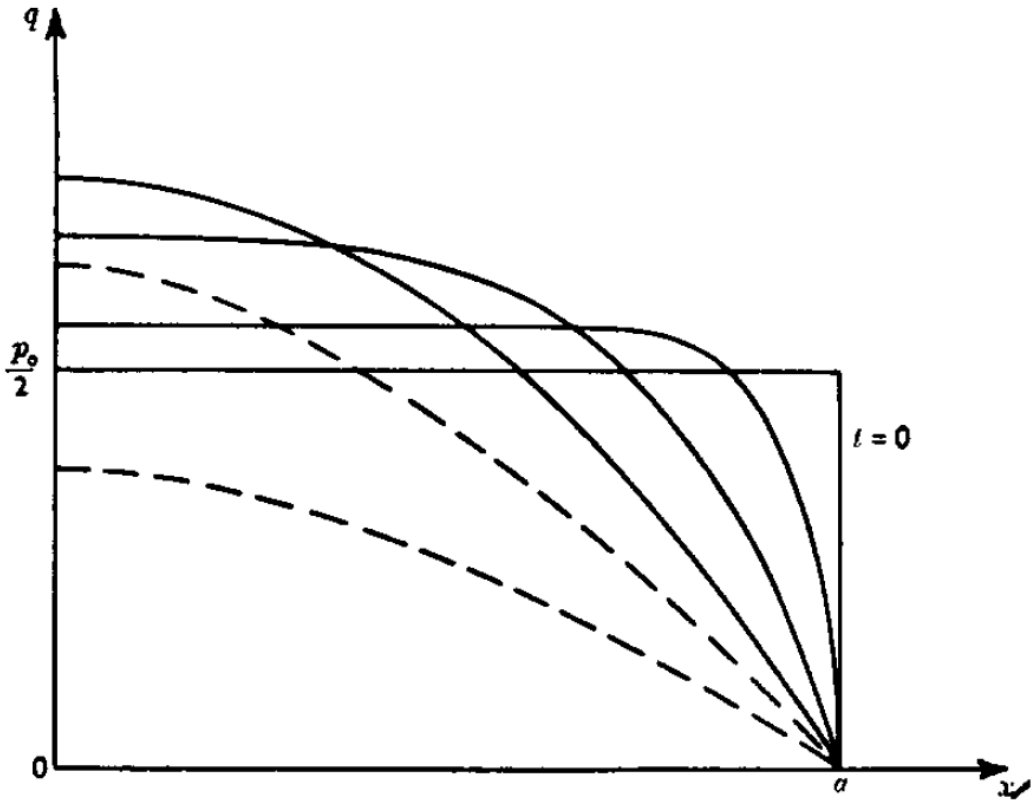

Figure 2-2. Chronological graph of Pressure (ordinate) against distance (abscissa) from the centre of the specimen , as reported by (Mandel, J., 1953), showing non-monotonic pressure response as explained by (Abousleiman et al., 1996).

In 1996, (Abousleiman et al., 1996) derived analytical solution to Mandel's problem to account for a special case of anisotropy known as transverse isotropy (also known as cross-anisotropy). As part of their solution, the magnitude of pore pressure along the x-axis (at any elevation z) was expressed as:

$$p(x,0) = \frac{F}{3a}\left[B_z + B_x \frac{M_{13}^u (M_{11}^u - M_{12}^u)}{M_{11}^u M_{33}^u - M_{13}^u M_{13}^u}\right] \tag{2.1}$$

Where 'B' is the Skempton's pore pressure coefficient generalized for anisotropy and expressed as:

$$B_x = \frac{3M(\alpha_x M_{33}^u - \alpha_z M_{13}^u)}{M_{33}^u (M_{11}^u + M_{12}^u) - 2M_{13}^u M_{13}^u} \tag{2.2}$$

$$B_z = \frac{3M(\alpha_z M_{11}^u + \alpha_z M_{11}^u - 2\alpha_x M_{13}^u)}{M_{33}^u(M_{11}^u + M_{12}^u) - 2M_{13}^u M_{13}^u} \tag{2.3}$$

and M_{ij}^u are the undrained elastic moduli that relate to their drained counterparts as:

$$M_{ij}^u = M_{ij} + \alpha_i \alpha_j M \tag{2.4}$$

Where 'M' is the Biot's modulus, and α_i are the anisotropic effective stress (Biot's) coefficients that, under assumption of microhomogeneity and microisotropy, can be expressed in terms of the undrained material properties as:

$$\alpha_x = 1 - \frac{M_{11} + M_{12} + M_{13}}{3K_s} \tag{2.5}$$

$$\alpha_z = 1 - \frac{2M_{13} + M_{33}}{3K_s} \tag{2.6}$$

2.2 Thermo-poroelasticity

The term 'poroelasticity' alone explains how pore fluid bears a portion of the stress applied to the porous medium (rock) and the resulting compression of the of the pores. Since temperature is another significant factor affecting the behavior of porous medium containing fluid, efforts have been made to expand the poroelastic equations to include temperature effects (Suárez-Arriaga, 2010). This can be achieved using Gibb's thermo-poroelastic potential or available enthalpy together with the skeleton's energy dissipation function (Coussy, 2004). In general, poroelasticity assumes an isothermal condition, while thermo-poroelasticity models constitute the more realistic non-isothermal behavior of subsurface formations.

2.3 Small Strain versus Large Strain

In elasticity theory of solid mechanics, small strain is assumed for solid deformation. Also known as the infinitesimal strain (or small deformation) theory, the small strain theory is a mathematical approach to the description of the deformation of a solid body in which the displacements are assumed to be much small than any relevant dimension of the body; therefore, the body's geometry and the constitutive material properties at each spatial point can be assumed to be unaltered by the deformation (Jon Jincai Zhan, 2020).

In most numerical modeling software for geomechanics, the default calculation mode is small strain. In a small strain mode, the gridpoints or particle positions do not change; therefore, calculations for stress and strain are performed using original shape of the zones. Such an assumption is acceptable given that the deformed shape is within some few percent of the original shape. In a large strain mode, however, grid points or positions are continually updated, and as a result, more accurate solution is obtained.
In other words, simulating in large strain mode provides more accurate representation of the real case, even though this comes at a cost of high computational effort. In some contemporary software, a user is able to balance between accuracy and the computational cost by specifying the frequency at which the positions and contacts are updated during the simulation run.
Therefore, the choice of small strain – large strain is wholly dependent on the behavior of the model. In situations where contacts are present and significant, or when parts are expected to more relative to one another, then large strain mode should be preferred for more accurate solution. Nevertheless, large strain and large displacement should not be confused, as if, for instance, displacement is distributed evenly throughout the model, then small strain assumption may still be valid.

2.4 EGS and Thermal Short-circuiting

Geothermal energy is a renewable energy that provides large energy source and can be recovered at several geologic locations across the globe. As at 2020, the total global installed geothermal capacity is 11,000 megawatts (Huttrer, 2020), which is only about 0.00025% of the Earth's total generating capacity (Stacey & Loper, 1988). This shows how great a potential of power out planet bears waiting to be exploited. Several countries are investing and benefiting from this geologic wealth, with the USA, Indonesia, the Philippines, Turkey, and New Zealand emerging as the leaders in installed capacity, accounting for over 65% of it. Efforts are ongoing by countries and the industry to increase this capacity, leading to the development of Enhanced Geothermal Systems (EGS), which aim at increasing heat transfer surface area and reservoir transmissivity via hydraulic fracturing, facilitating recovery of geothermal energy in rocks with low permeability (W. Tester and M. C. Smith, 1977).
Thermal short-circuiting is a term given in a situation in an EGS when the flowing working fluid tends to prefer nearer fracture flow paths due to low initial stress and large fracture opening, thereby decreasing thermal drainage volume, accelerating thermal breakthrough, and consequently aggravating the decline in recoverable heat energy. It is caused by two processes: a) flow-channeling and b) plane channeling (see Figure 2-3). A comprehensive work by (McLean & Espinoza, 2023) sought to explore this phenomenon as well as recommend four ways to prevent or mitigate it:

1. Avoid locations with high initial hydraulic aperture and high fracture compliance, most likely to occur in locations with low in-situ stresses.
2. Avoid losing contact of fracture asperities to limit the rapid increase of hydraulic aperture.
3. Use a reverse EGS doublet*, if possible, to mitigate thermal short-circuiting by avoiding plane-chanelling.
4. Optimize fracture spacing to balance viscous loss in wellbores (contributes to plane-channeling) and thermal and mechanical fracture interference (contributes to flow-channeling).

*as can be seen on Figure 2-4, reverse doublet is when the doublet (one injector and the other, producer) are designed in a way that the flow in both wells are in the same direction. This design helps avoid the occurrence of plane channeling, thereby reducing the effect of thermal short-circuiting.

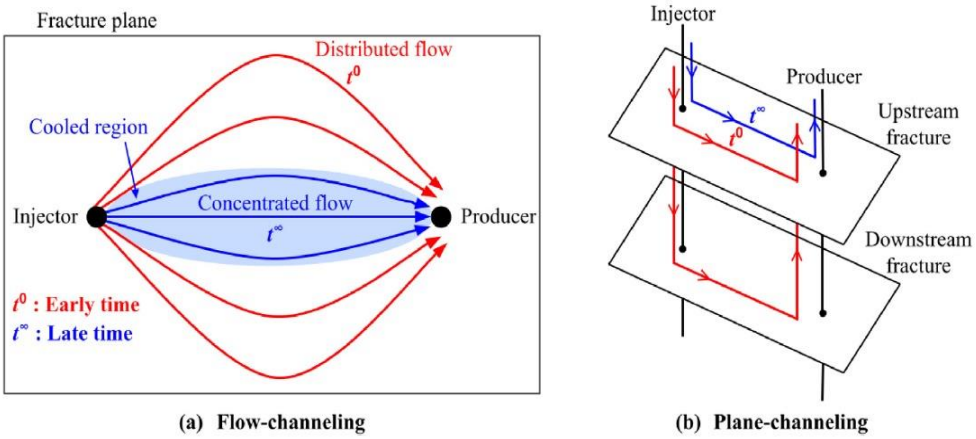

Figure 2-3. Figure showing the two processes that lead to thermal short-circuiting: a) Flow-channeling, in which fluid flow is distributed across fracture surfaces in early times, yet the transmissivity within the cooled region in increased by heat drainage, consequently causing the preferential flow path to converge to a small volume. b) Plane-channeling, which occurs when injection fluid is distributed throughout the EGS hydraulic network in early times, yet heat drainage and geometrical properties of the hydraulic network can cause a single fracture to flow majority of the injection fluid in later times. Figure adapted from (McLean & Espinoza, 2023).

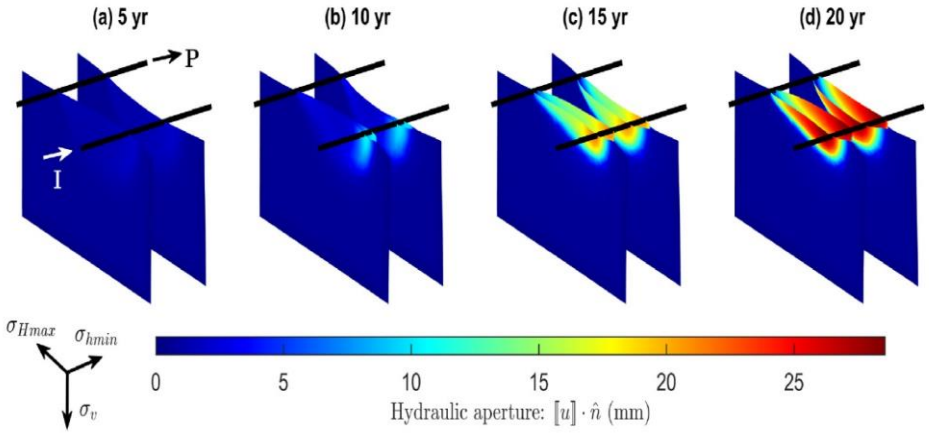

Figure 2-4. Figure showing graph of hydraulic aperture on a deformed configuration and how reverse doublet helps mitigate thermal short-circuiting by avoiding plane channeling. Fracture opening maintains similar feedback for both the upstream and downstream fractures since the reverse doublet prevents plane-channeling. Flow-channeling, nevertheless, is still observed as a result of large fracture opening displacements caused by the thermos-poroelastic response to heat drainage. Figure adapted from (McLean & Espinoza, 2023).

The next sub-section discusses foundational concepts upon which the model is built. First, it gives an overview of the two main components of poroelasticity: rock and fluid; then, the balanced equations (i.e. continuum equation, and mass and energy balances) are derived for a coupled thermo-poroelastic model.

2.5 Rock and Fluid Properties

The porous medium that accommodates the fluid flow at a depth within the earth is the known reservoir rock; in the real sense, it comprises an intricate network of voids (pores) within a solid material (rock). Fluid flow, therefore, only occurs within the interconnected pores of a given rock matrix. It is important to note that a more realistic treatment of the porous media would be to consider the flow mechanism at the molecular scale; however, the number of molecules existing in just a milliliter of fluid would make this approach almost impossible, considering time and computational cost. This essentially leads to the adoption of a more practical scale known as the Representative Elementary Volume (REV), in which the porous medium is treated as a continuum rather than a system of individual molecules interacting with the walls of the matrix (see Figure 2-5). As can be seen in work done by (Bear, J., 1988) among others, the EV aims at scaling the porous medium by a

reasonable number of pores, yet small enough to describe the fluid-rock interaction and flow processes.

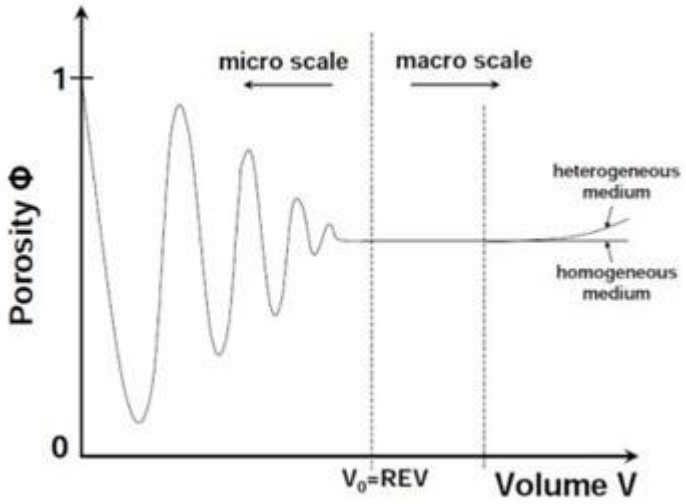

Figure 2-5. Graph showing the Representative Elementary Volume Criterion (Bear, J., 1988).

2.5.1 Porosity

Porosity of a porous medium is the ratio of the pore volume to the total rock volume. Symbolized with ∅, is most often expressed as a decimal (between 0 and 1). Depending on the method of measurement and purpose of application, porosity can be either total or effective. Total porosity (as expressed below) captures the total void space, whereas effective porosity represents the interconnected pores that contribute to fluid flow. A more detailed discussion of porosity is made in section 2.6.

$$\emptyset = \frac{V_{pore}}{V_{bulk}} \tag{2.7}$$

2.5.2 Permeability

Permeability is defined as the tendency of the porous matrix to allow flow of fluid. In other words, it is the measure of the degree to which fluid can flow within the porous medium. It depends on several other properties such as the size and geometry of the pores. Permeability is symbolized with K and measured in darcy (D) as a field

unit or meter squared as S.I. unit. One type of permeability, the intrinsic permeability, ascribes this property solely to the porous medium. Another form of permeability, the hydraulic conductivity (K_f), includes the contribution of the flowing fluid's own properties to the flow, as defined below:

$$K_f = K\frac{\rho g}{\mu} \tag{2.8}$$

Permeability is a tensor, which means it varies with the spatial direction or orientation of the flow or pore.

2.5.3 Saturation

Saturation is the measure of the fraction of the pore space occupied by a fluid phase (α), expressed as:

$$S_\alpha = \frac{V_\alpha}{V_{pore}} \tag{2.9}$$

The sum of saturations of the various phases is unity:

$$\sum_\alpha S_\alpha = 1 \tag{2.10}$$

2.5.4 Capillary Pressure

In porous media flow of immiscible fluids, there is a tendency of one fluid to adhere to the walls of the matrix, leaving the other fluid in the form of drops away from the walls. The former fluid is then termed to as the wetting phase, while the latter is the non-wetting phase. Capillary pressure is the pressure difference between the wetting phase and non-wetting phase as follows:

$$P_c = P_n - P_w \tag{2.11}$$

The above equation requires the measurement of the separate wetting and non-wetting phases' pressure, but this is only possible through analysis at the molecular scale; however, in 1964, Brooks and Corey developed a formulation that relates Pc to saturation, as expressed below:

$$P_c = P_e \left(\frac{S_w - S_{rw}}{1 - S_{rw}} \right)^{\frac{1}{\lambda_{BC}}} \tag{2.12}$$

P_e is the "entry" pressure, which is the pressure the non-wetting phase must attain in order to enter a unit volume fully saturated with the wetting phase. λ_{BC} is a coefficient that depends on grain size and distribution.

2.6 Geomechanics-Poroelasticity

As the name implies, poroelasticity entails the ability of the porous medium to expand, contract or deform under pressure. This means that the porosity of the rock is subject to frequent changes during injection or production as the stresses and, therefore, strains are altered by pressure. An essential relation between porosity and volumetric strain can then be derived by introducing the stress-strain relation into the expression of porosity change as illustrated in the following steps. It should be noted that the pore volume (V_p) in this derivation is regarded as the interconnected pore volume (Detournay & Alexander H.-D., Cheng, 1993) which excludes the isolated pores, thereby rendering the resulting porosity an effective porosity:

$$d\emptyset = \mathrm{d}\left(\frac{V_p}{V_b}\right) = \frac{V_b \, \mathrm{d}V_p - V_p \, \mathrm{d}V_b}{{V_b}^2} = \frac{dV_p}{V_b} - \emptyset \frac{dV_b}{V_b} \tag{2.13}$$

From $K = \frac{\sigma_v}{\varepsilon_v}$; and $\sigma' = \sigma - \alpha p$, therefore,

$$(d\varepsilon_v) = \frac{dV_b}{V_b} = -\frac{1}{K_{dr}} (d\sigma_v - \alpha dp) \tag{2.14}$$

where σ' is the effective stress and α is the Biot's coefficient defined as $\alpha = 1 - \frac{K_{dr}}{K_s}$

Equation (2.) can be written for the pore by introducing β, a dimensionless effective stress coefficient ((Detournay & Alexander H.-D., Cheng, 1993)), defined as $\beta = 1 - \frac{K_p}{K_s}$ so that

$$\frac{dV_p}{V_b} = -\frac{1}{K_p} (d\sigma_v - \beta dp) \tag{2.15}$$

Substituting (2.) and (2.) into (2.) or combining (2.), (2.) and $V_p = \emptyset V_b$ eventually gives a porosity-strain relation as illustrated in the following steps (the latter option is taken):

$$\frac{d\left(\frac{V_p}{\emptyset}\right)\emptyset}{Vb} = -\frac{1}{K_{dr}}(d\sigma_v - \alpha dp) \tag{2.16}$$

$$\frac{\emptyset dV_p - V_p d\emptyset}{\emptyset^2 V_p}\emptyset = -\frac{1}{K_{dr}}(d\sigma_v - \alpha dp) \tag{2.17}$$

$$\frac{dV_p}{V_p} = \frac{d\emptyset}{\emptyset} - \frac{1}{K_{dr}}(d\sigma_v - \alpha dp) \tag{2.18}$$

$$\therefore \mathrm{d}\emptyset = -\frac{1}{\mathrm{K_p}}\emptyset \mathrm{d}\sigma_\mathrm{v} + \frac{1}{\mathrm{K_p}}\beta\emptyset \mathrm{dp} + \frac{1}{\mathrm{K_{dr}}}\emptyset \mathrm{d}\sigma_\mathrm{v} - \frac{\alpha}{\mathrm{K_{dr}}}\emptyset \mathrm{dp} \tag{2.19}$$

$$d\emptyset = -\frac{1}{K_p}\emptyset d\sigma_v + \frac{1-\frac{K_p}{K_s}}{K_p}\emptyset dp + \frac{1}{K_{dr}}\emptyset d\sigma_v - \frac{1-\frac{K_{dr}}{K_s}}{K_{dr}}\emptyset dp \tag{2.20}$$

$$d\emptyset = \left(-\frac{\emptyset}{K_{dr}} + \frac{\emptyset}{K_p}\right)(-d\sigma_v + dp) \tag{2.21}$$

Employing $K_p = \frac{\emptyset}{\alpha}K_{dr}$ $(Detouray\ \&\ Chegg, 1993)$,

$$d\emptyset = \left(-\frac{\emptyset}{K_{dr}} + \frac{\alpha}{K_{dr}}\right)(-d\sigma_v + dp) \tag{2.22}$$

Finally, with $\frac{1}{K_s} = \frac{1-\alpha}{K_{dr}}$,

$$d\emptyset = \left(\frac{1}{K_{dr}}(1-\emptyset) - \frac{1}{K_s}\right)(-d\sigma_v + dp) \tag{2.23}$$

(Han & Dusseault, 2003), who made similar derivation but using compressibility instead of bulk modulus, further replace stress with volumetric strain, so we now have

$$d\emptyset = \left(1 - \frac{K_{dr}}{K_s} - \emptyset\right)(-d\varepsilon_v + \frac{1}{K_s}dp) \tag{2.24}$$

For the assumption of rigid grains ($K_s \to \infty$),

$$d\emptyset = -(1-\emptyset)d\varepsilon_v \tag{2.25}$$

$$\emptyset - \emptyset_o - = -(1-\emptyset)(\varepsilon_v - \varepsilon_{vo}) \tag{2.26}$$

Assuming zero initial strain,

$$\emptyset - \emptyset_o = -\varepsilon_v + \emptyset\varepsilon_v \;\Rightarrow\; \emptyset(1-\varepsilon_v) = \emptyset_o \tag{2.27}$$

$$\emptyset = \emptyset_{eff} = \frac{\emptyset_o - \varepsilon_v}{1-\varepsilon_v} \tag{2.28}$$

The difference at the denominator can be regarded as insignificant ($\varepsilon_v \ll 1$), simplifying the above equation to

$$\emptyset_{eff} = \emptyset_o - \varepsilon_v \tag{2.29}$$

CHAPTER 3

STATEMENT OF THE PROBLEM

The method of simulating a geothermal reservoir without considering geomechanics is questionable. This is because in reality, the porous medium is subject to stresses and strains that alter the shapes and orientation of the subsurface rocks with time; this process brings about a substantial change in porosity and permeability, thereby affecting the entire simulation results. This study will pinpoint the inaccuracy of the conventional (stress-independent) reservoir simulation method with graphical illustrations and by comparing with the coupled method for more accurate results. Thus, the study will confirm the dependence of porosity (and permeability) on the stress in a porous medium. Furthermore, results from 2-D and later (for a better representation of reality) 3-D numerical models of a geothermal reservoir will be employed to essentially demonstrate the impact of thermal stress and a potential thermal short-circuiting.

CHAPTER 4

METHODOLOGY

The methodology adopted to build and simulate the models presented in this work follows a general workflow illustrated on Figure 4-1. The presented workflow is strictly followed to avoid any miscalculations that would pave way to misrepresentations. Each stage of the workflow is of equal importance, and the problem at hand undergoes all the stages in order to determine the right approach to its solution.

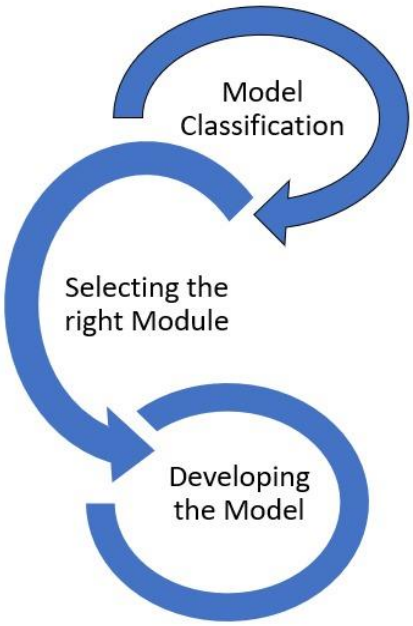

Figure 4-1. Workflow illustrating the methodology employed to build and simulate a coupled model.

4.1 Model Classification

Initially, the model at hand is evaluated to determine its inherent features and components. For our case, a model generally falls under one of the following categories:

1. Mechanical.

2. Poro-elastic (i.e. hydro-mechanical).
3. Thermo-poroelastic (i.e. thermo-hydromechanical).

The next classification, then, has to do with the dimension of the model:

1. One-dimensional (1-D)
2. Two-dimensional (2-D)
3. Three-dimensional (3-D)

4.2 Selecting the Right COMSOL Modules and Interfaces

After classifying the model, we are now set to employ the right set of modules needed to build our model. It should be noted that once a model requires more than one constitutive interface, then an additional (suitable) coupling interface needs to be added in order to update all affected variables due to coupling.
Table 4-1 shows examples of such coupling modules for specific combination of constitutive modules.

Table 4-1. The right coupling interfaces for combination of constitutive modules

Model classification	**Constitutive module, & (interface(s))**	**Coupling interface**
Poro-elastic	1. Porous media and subsurface flow, (Darcy's law) 2. Structural mechanics, (Solid Mechanics)	Poroelasticity
Thermo-poroelastic	1. Porous media and subsurface flow, (Darcy's law) 2. Structural mechanics, (Solid Mechanics) 3. Porous media (Heat transfer in porous media)	- Poroelasticity (for coupling 1 & 2) - Thermal expansion (for coupling 2 & 3)

4.3 Developing the Model

Then, finally, we arrive at the stage where the actual work will be done. This stage encompasses building the entire model from scratch: from specifying the geometry and dimensions of the model, to selecting the right materials (solid, fluid etc.), to inputting the values of the mechanical, thermal, chemical properties, etc. where applicable. Fortunately, COMSOL comes in quite handy; it has plethora of in-built libraries from which most of such materials (and their properties, for that matter) can be found.

CHAPTER 5

MATHEMATICAL MODELING: GEOMECHANICS AND FLUID FLOW IN POROUS MEDIA

The geomechanics and fluid flow processes in the porous media are modelled by powerful simulators, which effectively do so by solving the non-linear partial differential mass and momentum balance equations numerically. The mass balance equations of the flow and the momentum balance equation of the geomechanics are obtained using the relations of the physical concepts illustrated in the previous chapter. Depending on the objective of the model, two different approaches to do this, as observed from previous studies, will be discussed. This chapter focuses on two things: first, to illustrate the balanced equations and other constitutive equations involved in the modelling and second, to analyze various reservoir cases using the models.

5.1 Mass Balance Equations

For a given porous media, the mass balance equation (also known as the continuity equation) is a mathematical expression of mass conservation in a control volume within the medium. In other words, the change in mass of fluid in a unit volume of the medium is only effected by fluxes at the boundary or an existing source or sink withing the volume, as shown below:

$$\frac{\partial(\emptyset\rho)}{\partial t} + \nabla \cdot (\rho v) = q \tag{5.1}$$

The equation above is written for one-phase flow, which is applicable for our models in this work. However, for a multi-phase case, specifically two-phase flow, the following equation is applied to indicate the distinct properties of the fluids involved:

$$\frac{\partial(\emptyset S_\alpha \rho_\alpha)}{\partial t} + \nabla \cdot (\rho_\alpha v) = q_\alpha, \tag{5.2}$$

where α represents wetting or non-wetting phase.

The velocity v in the flux term can be substituted with its relation from Darcy equation, in which

$$v = -\frac{k}{\mu}(\nabla p - \rho g), \tag{5.3}$$

where $'\rho g'$ accounts for the effect of gravity on the flow. Equation 4.10 can therefore be re-written as

$$\frac{\partial(\emptyset\rho)}{\partial t} - \nabla \cdot [\rho\frac{k}{\mu}(\nabla p - \rho g)] = q \tag{5.4}$$

A closer look at the above combined momentum balance (Darcy equation)—mass balance equation for single-phase flow, specifically the storage term, leads to a further derivation of the storage coefficient as demonstrated below:
Assuming negligible hydraulic gravitational gradient $(\nabla p \gg \rho g)$, we reduce the equation to

$$\frac{\partial(\emptyset\rho)}{\partial t} - \nabla \cdot (\rho\frac{k}{\mu}\nabla p) = q \tag{5.5}$$

This done, we now take partial derivatives of the storage term as follows:

$$\rho\frac{\partial\emptyset}{\partial t} + \emptyset\frac{\partial\rho}{\partial t} - \nabla \cdot (\rho\frac{k}{\mu}\nabla p) = q \tag{5.6}$$

$$\Rightarrow \rho\frac{\partial\emptyset}{\partial p}\cdot\frac{\partial p}{\partial t} + \emptyset\frac{\partial\rho}{\partial p}\cdot\frac{\partial p}{\partial t} - \nabla \cdot (\rho\frac{k}{\mu}\nabla p) = q \tag{5.7}$$

$$\Rightarrow \left(\rho\frac{\partial\emptyset}{\partial p} + \emptyset\frac{\partial\rho}{\partial p}\right)\cdot\frac{\partial p}{\partial t} - \nabla \cdot (\rho\frac{k}{\mu}\nabla p) = q \tag{5.8}$$

$$\Rightarrow \rho\cdot\emptyset\left(\frac{1}{\emptyset}\frac{\partial\emptyset}{\partial p} + \frac{1}{\rho}\cdot\frac{\partial\rho}{\partial p}\right)\cdot\frac{\partial p}{\partial t} - \nabla \cdot \left(\rho\frac{k}{\mu}\nabla p\right) = q, \tag{5.9}$$

From which the storage coefficient (S) is extracted as

$$S = \frac{1}{\emptyset}\frac{\partial\emptyset}{\partial p} + \frac{1}{\rho}\cdot\frac{\partial\rho}{\partial p}, \qquad [Pa^{-1}] \tag{5.10}$$

Where, the first and second terms on the right hand-side represent rock and fluid compressibility, respectively.

5.2 Momentum Balance Equation

Assuming a quasi-static condition, and thereby making all time derivatives insignificant, the conservation of momentum is expressed as:

$$\nabla \cdot \sigma + \rho g = 0, \tag{5.11}$$

where 'g,' even though reduced to gravity vector, is generally used to represent all body forces in the system. Re-introducing the two-phase case, and considering the respective densities of each phase, we can define a bulk density (ρ_b) as:

$$\rho_b = (S_w \rho_w + S_n \rho_n)\emptyset + \rho_m(1 - \emptyset) \tag{5.12}$$

Furthermore, we have earlier seen a relation of effective stress with pore pressure as:

$$\sigma' = \sigma - pI \tag{5.13}$$

Again, instead of 'p,' we apply an effective pore pressure (p_{eff}) to represent the contribution of the two phases as

$$p_{eff} = S_w p_w + S_n p_n \tag{5.14}$$

Then, equation (5.) is modified as

$$\nabla \cdot (\sigma' + p_{eff} I) + \rho_b g = 0 \tag{5.15}$$

For easy application, we linearize the above equation by subtracting the initial values of stress, pressure and density as:

$$\Delta\sigma' = \sigma' - \sigma_i' \tag{5.16}$$

$$\Delta\rho_b = \rho_b - \rho_{b,i} \tag{5.17}$$

$$\Delta p_{eff} = p_{eff} - p_{eff,i} \tag{5.18}$$

This then leads to

$$\nabla \cdot (\Delta\sigma' + \Delta p_{eff} I) + \Delta\rho_b g = 0 \tag{5.19}$$

Also, $\Delta\rho_b$ is expanded as

$$\Delta\rho_b = \Delta\emptyset(S_w\rho_w + S_n\rho_n) + \emptyset\Delta(S_w\rho_w + S_n\rho_n) + \Delta\rho_m(1-\emptyset) + \rho_m\Delta(1-\emptyset) \tag{5.20}$$

Then, assuming negligible porosity change and constant rock matrix density,

$$\Delta\rho_b \approx \emptyset[\Delta S_n(\rho_n - \rho_w) + S_n\Delta\rho_n] \tag{5.21}$$

Finally, we have the momentum balance equation simplified as

$$\nabla\cdot(\Delta\sigma' + \Delta p_{eff}I) + \emptyset[\Delta S_n(\rho_n - \rho_w) + S_n\Delta\rho_n]\cdot g = 0 \tag{5.22}$$

Sub-sections 5.1and 5.2 describe one of two approaches mentioned at the beginning of this section. The objective in this approach is to analyze the effect of rock matrix deformation on porosity and permeability. Therefore, with this approach, the porosity and permeability values are updated at each time step using the calculated strain (via displacement vector, u) at that step.
The next subsection presents the other approach, which solely focuses on the effect of pore pressure on deformation (displacement).

5.3 Pressure-strain Approach

We may also call this approach the poroelastic approach since it specifically describes the poroelastic behavior of the porous media, without accounting for any effects on porosity and permeability. At each time step, therefore, the displacement vector (u) is updated with the current pressure head. With the expression for storage coefficient (S) above (5.), equation (5.) can be simplified as:

$$\rho\cdot\emptyset S\cdot\frac{\partial p}{\partial t} - \nabla\cdot\left(\rho\frac{k}{\mu}\nabla p\right) = q \tag{5.23}$$

The product $\emptyset S$ is known as 'poroelastic storage, S_p,' which is the inverse of Biot's modulus (M) and can be expressed as:

$$S_p = \frac{\emptyset}{K_f} + \frac{\alpha - \emptyset}{K_s} \tag{5.24}$$

It should be noted that the above expression for S_p is obtained when an ideal (isotropic porous) material undergoes Π-loading, where porosity remains constant (Detournay & Alexander H.-D., Cheng, 1993). Furthermore, the mass source/sink q can be expressed using poroelastic parameters under small strain condition as:

$$q = -\rho\alpha\frac{\partial\varepsilon}{\partial t} \tag{5.25}$$

Then the mass balance equation finally assumes a new form

$$\rho \cdot \mathrm{S}_p \cdot \frac{\partial p}{\partial t} - \nabla \cdot \left(\rho \frac{k}{\mu} \nabla p \right) = -\rho \alpha \frac{\partial \varepsilon}{\partial t} \tag{5.26}$$

The right hand-side of the above equation is can also be interpreted as a coupling term from the geomechanics part, and the negative sign implies a sink: it represents time rate of expansion of the porous medium, meaning that the space (volume fraction) available for the fluid increases, which is why the sign is reversed. The deformation of the porous matrix is described using the following equation:

$$-\nabla \cdot \sigma = \rho g \tag{5.27}$$

As mentioned earlier, the above equation is time-independent due to the quasi-static nature of the solid matrix. In this approach, the above equations are solved with pre-defined boundary conditions to simulate the flow process in a poroelastic material such as the porous medium. Equation (5.) can be expressed (as a linear constitutive law) in a 2-D tensorial form as:

$$\begin{bmatrix} \sigma_{xx} \\ \sigma_{yy} \\ \sigma_{xy} \end{bmatrix} = \frac{E}{(1+\nu)(1-2\nu)} \begin{bmatrix} 1-\nu & \nu & 0 \\ \nu & 1-\nu & 0 \\ 0 & 0 & 1-2\nu \end{bmatrix} \begin{bmatrix} \varepsilon_{xx} \\ \varepsilon_{yy} \\ \varepsilon_{xy} \end{bmatrix} - \begin{bmatrix} \alpha p & 0 & 0 \\ 0 & \alpha p & 0 \\ 0 & 0 & \alpha p \end{bmatrix} \tag{5.28}$$

Where σ_{xx} and σ_{yy} are principal stresses in the x and y directions, respectively,
ε_{xx} and ε_{yy} are principal strains
σ_{xy} – shear stress
ε_{xy} – shear strain
E - Young's modulus
ν – Poisson's ratio
α – Biot's coefficient
p – pore pressure
It should be noted that $\frac{E}{(1+\nu)(1-2\nu)} \begin{bmatrix} 1-\nu & \nu & 0 \\ \nu & 1-\nu & 0 \\ 0 & 0 & 1-2\nu \end{bmatrix}$ is sometimes known as 'stiffness matrix, denoted 'D.'
The poroelasticity module of the COMSOL software solves equations (5.) and (5.) together to simulate the poroelastic behavior of a porous medium. Specifically, it models coupled fluid flow and geomechanics process, laying more emphasis on the effect of fluid pressure changes on deformation (strain) of the porous medium.

5.4 Thermal Effect

So far in this work, we have treated all flow and geomechanics processes in an isothermal domain. However, in a more realistic sense, the porous media in

subsurface structures and the ongoing processes occur in a non-isothermal environment, and studies have shown the significance of temperature effects on the poroelastic matrix, thereby leading to a yet novel area of focus known as thermos-poroelasticity. Effects of temperature are especially crucial in geothermal heat extraction, nuclear waste storage, carbon capture and storage (CCS), and steam injection during thermal oil recovery. (McLean & Espinoza, 2023) clearly demonstrated how temperature variations can lead to induced stresses (typically known as thermal destressing), which in turn have an immense impact on the fracture dynamics as well as recovery factor and productivity. In a thermo-poroelastic case, the effect of temperature in both the mass and momentum balance become obvious as illustrated below.

$$\sigma_{ij} = \left(K - \frac{2G}{3}\right)\delta_{ij}\varepsilon_{ii} + 2G\varepsilon_{ij} - \alpha\delta_{ij}p - \beta_d K\delta_{ij}T \tag{5.29}$$

$$\zeta = \alpha\varepsilon_{ii} + \frac{p}{M^*} - \beta_e \tag{5.30}$$

Where,
σ: Cauchy stress tensor
K: drained bulk modulus
G: shear modulus
δ_{ij}: the Kronecker delta
ε_{ii}: volumetric strain
p: pore fluid pressure
β_d: drained volumetric thermal expansion of the porous domain
T: temperature
ζ: variation in fluid content
M^*: the Biot modulus
β_e: volumetric thermal expansion for variation in fluid content (at constant volume, i.e. for $\varepsilon_{ii} = p = 0$)

ζ is a fluid-related strain defined as the amount of fluid entering the solid domain per unit volume of the solid domain. $\zeta > 0$ for fluid entering the solid domain.
In the tensorial form, equation (5.) can be expressed as:

$$\begin{bmatrix}\sigma_{xx} & \sigma_{xy} & \sigma_{xz}\\ \sigma_{yx} & \sigma_{yy} & \sigma_{yz}\\ \sigma_{zx} & \sigma_{zy} & \sigma_{zz}\end{bmatrix} = \left(K - \frac{2G}{3}\right)\begin{bmatrix}\varepsilon_{xx} & 0 & 0\\ 0 & \varepsilon_{yy} & 0\\ 0 & 0 & \varepsilon_{zz}\end{bmatrix} + 2G\begin{bmatrix}\varepsilon_{xx} & \varepsilon_{xy} & \varepsilon_{xz}\\ \varepsilon_{yx} & \varepsilon_{yy} & \varepsilon_{yz}\\ \varepsilon_{zx} & \varepsilon_{zy} & \varepsilon_{zz}\end{bmatrix} - \begin{bmatrix}\alpha p & 0 & 0\\ 0 & \alpha p & 0\\ 0 & 0 & \alpha p\end{bmatrix} - \begin{bmatrix}\beta_d KT & 0 & 0\\ 0 & \beta_d KT & 0\\ 0 & 0 & \beta_d KT\end{bmatrix} \tag{5.31}$$

It should be noted that the above tensorial expression can be split into volumetric and deviatoric parts, where the latter (shear stress) is independent of the pore pressure.

Considering the mean total stress $\sigma_m = \frac{\sigma_{ii}}{3} = tr(\sigma_{ij})/3$ and volumetric strain $tr(\varepsilon_{ij})/3$, equation (5.) reduces to:

$$\sigma_m = K\varepsilon_{ii} - \alpha p - \beta_d KT \tag{5.32}$$

where the (drained) volumetric thermal expansion of the homogenous poroelastic solid matrix, β_d, is equal to three times the linear thermal expansion.
Furthermore, the volumetric thermal expansion for variation in fluid content is expressed as:

$$\beta_e = \alpha\beta_d + \phi(\beta_f - \beta_d) \tag{5.33}$$

Where ϕ is the porosity of the rock and β_f is the volumetric thermal expansion of the fluid. The Biot modulus, M^*, is related to the change in variation in fluid content per unit change in pore fluid pressure as:

$$M^{*-1} = \frac{\partial \zeta}{\partial p}|_{\varepsilon_{ii}} = \frac{\phi}{K_f} + \frac{\alpha - \phi}{K_s} \tag{5.34}$$

Where K_f and K_s are the bulk modulus of the fluid and (porous) solid matrix, respectively.
The Biot's coefficient is an expression of the change in the mean total stress per unit change in pressure at constant bulk volume:

$$\alpha = \frac{\partial \sigma_m}{\partial p}|_{\varepsilon_{ii}} = 1 - \frac{K}{K_s} \tag{5.35}$$

For a rock matrix with fully interconnected porosity. Note that the Biot coefficient is solely dependent on the properties of the matrix skeleton and is by no means affected by fluid properties.
It also important to note that as temperature changes, most materials tend to change volume in response. Therefore, even with a slight temperature variation, the resulting stress in a constrained structure can be substantial. The constitutive equation therefore can be modified to include the thermal strain as follows:

$$\sigma = C:(\varepsilon - \varepsilon_{th}), \tag{5.36}$$

Where C is the stress-strain relation tensor, ε is the total strain and ε_{th} is the thermal strain. More detailed analysis of the thermal strain is conducted in section

5.5 Energy Balance

In our case, the heat transfer in a porous media for both solid and fluid phases can be mathematically expressed with the local thermal equilibrium hypothesis

$$(\rho C_p)_{eff} \frac{\delta T}{\delta t} + \rho_f C_{p,f} \boldsymbol{u} \cdot \nabla T + \nabla \cdot \boldsymbol{q} = Q \tag{5.37}$$

$$\boldsymbol{q} = -k_{eff} \nabla T \tag{5.38}$$

Where,
ρ_f – density of fluid
k_{eff} – effective thermal conductivity (a scalar in our case, or a tensor given an anisotropic thermal conductivity) is related to the conductivity of the solid k_s and the fluid k_f and depends on the geometry of the medium. A general formula $k_{eff} = \rho_f C_{p,f} \boldsymbol{u}$
$C_{p,f}$ – fluid heat capacity at constant pressure
$\boldsymbol{q}$ – conductive heat flux
T – temperature
t – time
$(\rho C_p)_{eff}$ - effective volumetric heat capacity at constant pressure, expressed as $(\rho C_p)_{eff} = \theta_s \rho_s C_{p,s} + \emptyset \rho_f C_{p,f}$, where
$\emptyset$ - porosity
θ_s – solid matrix volume fraction (1-$\emptyset$)
$\boldsymbol{u}$ – the velocity field, which can also be interpreted as Darcy velocity, i.e. the volume flow rate per unit cross sectional area.
The velocity within the pore (the average linear velocity can be computed as

$$\boldsymbol{u}_f = \boldsymbol{u}/\emptyset \tag{5.39}$$

Where $\emptyset$ is the fluid's volume fraction, an equivalent of porosity.
Q – heat source or sink
The effective thermal conductivity (k_{eff}) is related to the conductivity of the solid k_s and the fluid k_f and depends on the geometry of the medium. A general formula defining conductivity is:

$$k = \frac{Qd}{A\Delta T} \tag{5.40}$$

Where

Q – amount of heat to transferred
d – distance between the two isothermal planes
A - surface area
ΔT – temperature difference
The following assumptions were applied:
The variables involved are defined as follows:
For higher accuracy and practicability, the presented governing partial differential equations are solved using numerical approach, as an analytical solution for such a thermo-hydromechanical behavior of saturated rock is quite complex and challenging even for the simplified conditions and virtually impossible for the real and general boundary and initial boundary conditions. The numerical solution is obtainable using methods such as finite element, finite difference or boundary element methods, and discretization of the model is made both in space (spatial) and time (temporal).

CHAPTER 6

NUMERICAL TEST EXAMPLES

6.1 Preliminary tests

We begin this section by presenting a number of models developed and run while analyzing the underlying concepts and equations as integrated in COMSOL to better understand the functionality of related modules.

6.1.1 Thermal strain test

This test is carried out to investigate the relationship between total strain and thermal strain in an elastic rectangular specimen with dimensions $100m \times 10m$, subject to axial load and/ or heat. This two-dimensional specimen is assumed to be a slice of the Rotokawa Geothermal Reservoir rock, located in Taupo Volcanic Zone, New Zealand; therefore, most of the thermoelastic properties are mean values of the real field, adopted from Siratovich et al., 2015. Figure 6-1 shows three scenarios that were tested. The three scenarios are each subject, respectively to mild, intense and moderate heat. A load of 1MPa is applied in scenarios 1 and 2 in the specified direction, while in scenario 3, the two ends of the specimen are fixed. Table 6-1 provides details of the properties involved. The mechanical and thermal components were coupled using COMSOL's 'thermal expansion' coupling module, and each scenario was run for 10 years.

Table 6-1. Model properties for thermal strain test

Property	**Value**	**Unit**
Young's modulus	31.8	GPa
Poisson's ratio	0.215	-
Initial temperature	373.15	K
Heat source (mild*, moderate, intense)	$4.5 \times (10^{-6}, 10^{-2}, 10^{-1})$	W/m^3
Thermal expansion coefficient	8.6×10^{-6}	$1/K$
Thermal conductivity**	3.75	W/m/K
Heat capacity***	723.5	J/kg/K

*Adopted from (Yang et al., 2023), ** Adopted from (García-Noval et al., 2024) ,
***Adopted from (Michael J. Heap et al., 2020).

The total strain can be expressed as follows:

$$\varepsilon_{tot} = \varepsilon_F + \varepsilon_{th} \quad (6.1)$$

From the above equation, we understand that the applied axial load and temperature are the only contributors to the straining of the specimen.

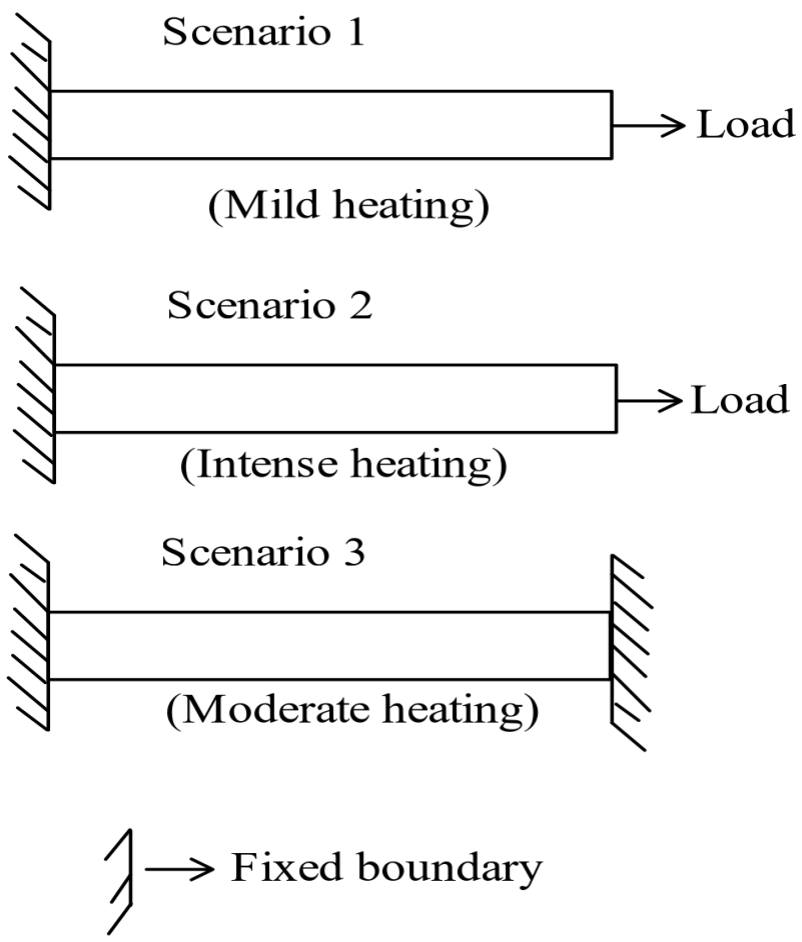

Figure 6-1. Diagram of three scenarios tested for thermal strain.

6.1.2 Simplified 3-D Model

We proceed to present another model as part of the preliminary study. This is a simplified Enhanced Geothermal System (EGS) with no fractures as shown on Figure 6-2. Two wells traverse the system at the center – one injecting 'cold' water at $313.15K$ with a line mass source value of 1kg/m/s and the other producing hot water at the same rate. The initial reservoir temperature is $373.15K$, and the heat source is input as:

$$Q_l = massflux \times ht.porous.fluid.Cp(313.15K - T) \tag{6.2}$$

Where, Q_l, the line heat source, is in W/m, and ht.porous.fluid.Cp is the fluid heat capacity. Table lll gives more details of the model properties.

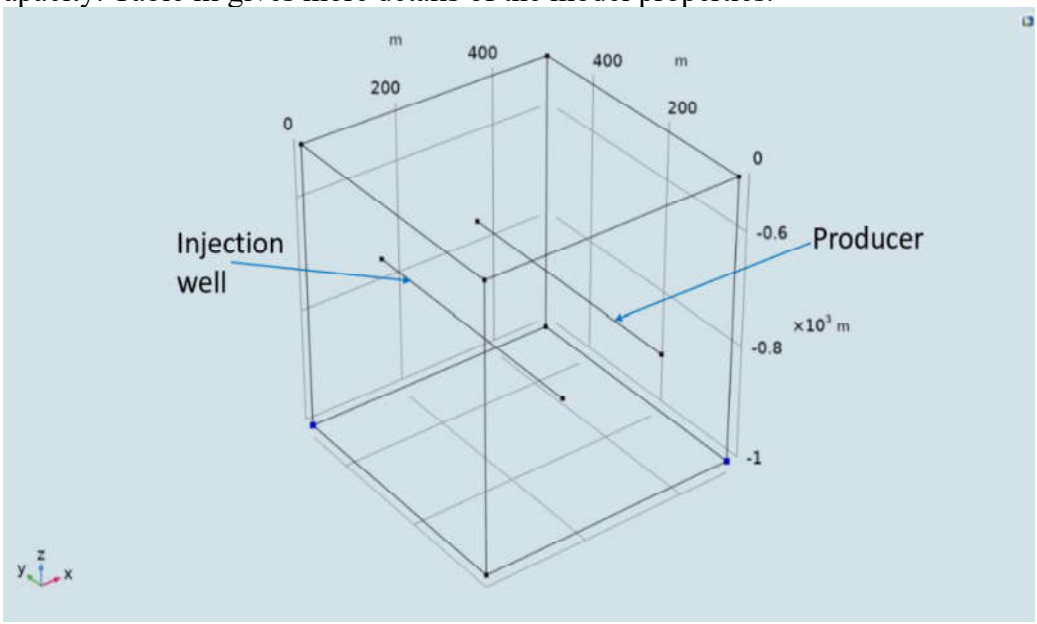

Figure 6-2. Simplified 3-D EGS model for preliminary studies

The model is discretized in 16500 elements and run for 10 years; the next chapter (Chapter 7) shows the results of the simulation.

Table 6-2. Properties of simplified EGS model

Property	**Value**	**Unit**
Young's modulus	800	MPa
Poisson's ratio	0.25	-
Porosity	0.19	-
Rock density	2600	kg/m^3
Permeability	1×10^{-14}	m^2
Rock's thermal conductivity	1.25	W/m/K

Heat capacity of rock	2230.77	J/kg/*K*

6.2 Sample Problems for Validation

This section is a preliminary stage of the main work, where we validate our model using proven theorems in geomechanics (specifically Terzaghi's one-dimensional consolidation theorem and the Biot's poroelasticity theorem studied by Mandel and Cryer).

6.2.1 Terzaghi's 1-D consolidation problem

To begin with, consider a 1m×10m rectangular specimen fixed at the bottom and two sides in normal directions. The top boundary is fully drained while the remaining three sides are assumed to be impermeable. Initially, a uniform load of 0.1MPa (~14.5psi) is suddenly applied to the top boundary, which instantaneously generates a pore pressure p that, as a standard condition, decreases in time. This example is a benchmark problem in poroelasticity and was first proposed by Carl von Terzaghi in 1923 (see Wang, 2000). Figure 6-3 and Table 6-3 illustrate the schematic diagram and the parameters used in this model, respectively.

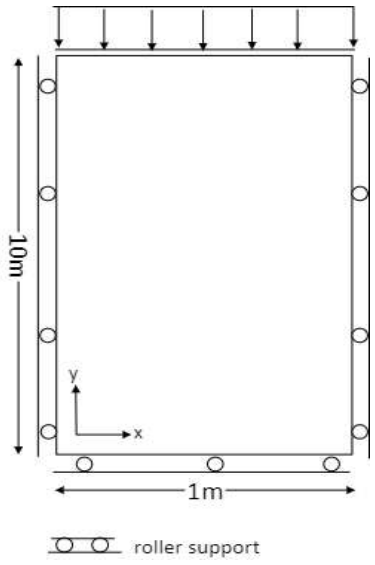

Figure 6-3. Diagram set up of Terzaghi's one-dimensional consolidation problem. The bottom, left and right boundaries are assigned roller support, meaning zero displacement in a direction normal to each boundary. The top boundary is subject to a sudden uniform load of approximately 14.5 psi. Credit to (Teichtmeister et al., 2019)

Table 6-3. Parameters for sample validation problems

Shear modulus	98.0 MPa
Poisson's ratio	0.3
Fluid density	1000.0 kg/m^3
Biot's modulus	20000.0 MPa
Biot's coefficient	1.0
Hydraulic conductivity	6.78×10^{-3} m/s

6.2.2 The Mandel-Cryer Effect

Next, we present the Mandel-Cryer effect, another well-known criterion used by geotechnical engineers for numerical model verification. As the name suggest, this effect was first observed by Mandel (Mandel, J., 1953) while analyzing the pressure changes in an infinitely long rectangular specimen sandwiched at the top and bottom by two frictionless plates (Abousleiman et al., 1996) as shown on Figure 6-4. Cryer (Cryer, 1963) made a similar observation in a at the center of a sphere of soil. In both cases, they observed, contrary to Terzaghi's, that pressure in areas far from the boundaries tend to build up initially before later dissipating through the boundaries. In this example, we model the Mandel's problem, where a specimen with dimensions $a = 100m \; and \; b = 30m$ is subject to a constant load of 40MN, normal to the two plates. The lateral sides are free from normal stress, shear stress and pore pressure, while the top and bottom boundaries are impermeable. Table 6-4 shows the homogenized properties of the specimen.

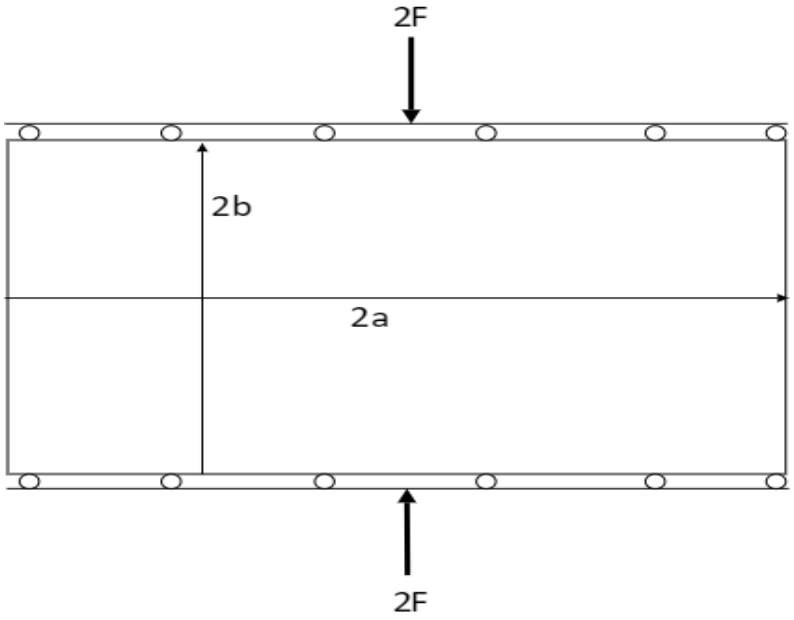

Figure 6-4. Model set-up of Madel-Cryer effect

Table 6-4. Homogenized properties of Mandel-Cryer problem

Density of porous medium	2750 $\mathrm{kg/m^3}$
Porosity	0.25
Fluid compressibility	$4 \times 10^{-10}\ Pa^{-1}$
Young's modulus	800 MPa
Poisson's ratio	0.3

6.2.3 Thermo-poroelastic model: Aktan & Ali's Problem

In this model, we consider a reservoir located in an infinitely large medium as proposed by (Aktan & Ali, 1978). Such a set-up allows the reservoir to both expand freely in all directions and be constrained at the boundaries by the layers over and beneath, thereby enabling a more accurate simulation of the pressure (loading) and displacement boundary conditions. The entire medium spans $137.16\mathrm{m} \times 82.30\mathrm{m}$ while the centered reservoir section measures $27.43m \times 9.14m$ as shown on Figure 6-5. Note the number of finite elements used by Aktan and Ali to discretize the system, as compared with ours discussed in section 7.1. The data given on Table 6-5 is used to run the model for 200 days at intervals of 1 day. Water injection is made at $560.93K$ along the left boundary of the reservoir at a constant pressure of 15.17 MPa. Production is made along the opposite side at 13.79 MPa. The top and bottom of the reservoir are assigned no-flow boundaries.

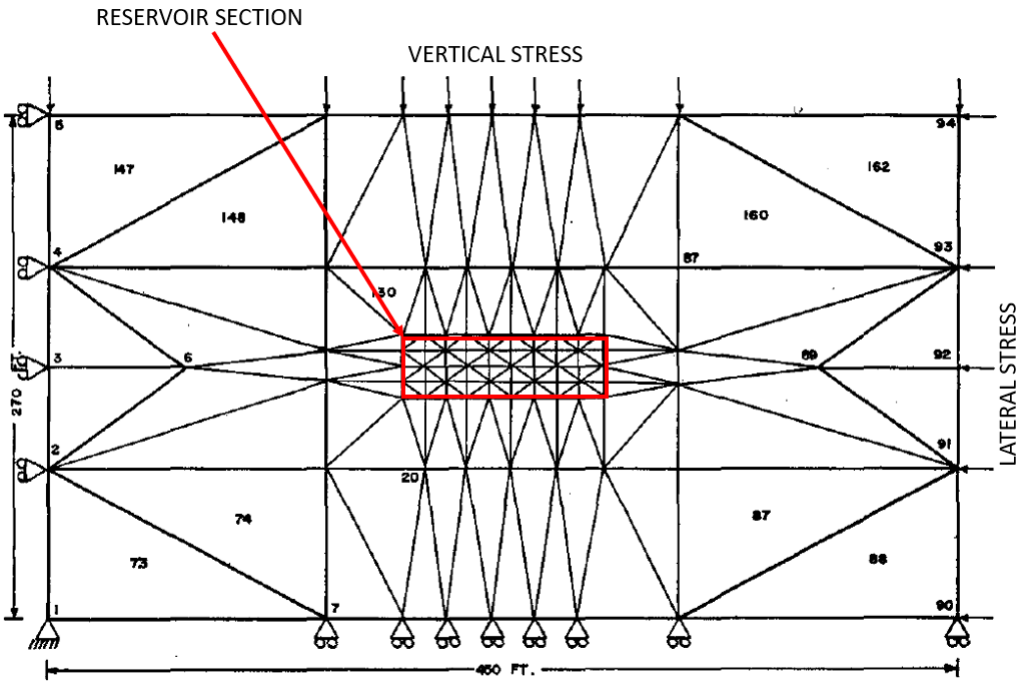

Figure 6-5 Finite element mesh of the System with 92 nodal points and 162 triangular elements , as defined by (Aktan & Ali, 1978).

Table 6-5.Model properties as defined by (Aktan & Ali, 1978)

		SI UNITS
Initial reservoir pressure, psi	2,200	15.17 MPa
Initial reservoir temperature, °F	100	310.93 K
Rock properties (of a Berea sandstone)		
Density, lbm/ft^3	148.95	2385.95 kg/m^3
Thermal conductivity, Btu/D-ft-°F	35	2.52 W/m/K
Specific heat, Btu/lbm-°F	0.2	836.8 J/kg/K
Total Compressibility, psi^{-1}	10×10^{-6}	$1.45 \times 10^{-10}\ Pa^{-1}$
Porosity, %	18.67	
Absolute permeability, darcy	0.089	$8.78 \times 10^{-13} m^2$
Coefficient of thermal expansion, $°F^{-1}$	15×10^{-6}	$2.7 \times 10^{-5}\ K^{-1}$
Water properties		
Density as STP, lbm/ft^3	62.4	999.6 kg/m^3
Specific heat, Btu/lbm-°F	1	4184 J/kg/K
Coefficient of thermal expansion, $°F^{-1}$	490×10^{-6}	$8.82 \times 10^{-4}\ K^{-1}$
Injection temperature, °F	550	560.93 K
Compressibility, psi^{-1}	3×10^{-6}	$4.50 \times 10^{-10} Pa^{-1}$

6.3 Simulating a Coupled 2-D Model of an EGS

We now develop a 2-D model of a fractured Geothermal System for detailed analysis. As shown on Figure 6-6, this porous medium spans $500m \times 500m$ with two horizontal fractures of varying apertures that depend on the average resultant displacement of the matrix relative to the fractured zones. The four outer boundaries of the domain were assigned "no flow." Moreover, the side boundaries were assigned "roller," meaning, displacement normal to the boundaries is zero, while the top and bottom boundaries were "free" to displacement in both directions. Table 6-6 gives details of the model's properties. Note that the model is assigned averaged values of the Rotokawa Andesite Geothermal Field as introduced in 6.1.1 (Paul A. Siratovich et al., 2014; Siratovich et al., 2015). The reservoir is assumed to be thermally insulated at the outer boundaries. Two vertical wells completely traverse the reservoir. Injection is made through the left-hand-side well at $333.15K$ while heated water is produced via the right-side well at a fixed zero pressure. For more accurate simulation results, the entire domain was subject to 'Physics-controlled' mesh of 'fine' sizes, generating 2116 elements over a mesh area of $250{,}000.0m^2$ (see Figure 6-7). The model was thermo-hydro-mechanically coupled using appropriate coupling models available on COMSOL. We finally ran the model for 10 years ($3.1557 \times 10^8\ seconds$); results were obtained after 87 timesteps at an average runtime of 1.5 minutes.

It should be noted that as simplistic approach to make up for the lack of a realistic fracture for such a coupled model, the fracture aperture is modeled as a function of its average deformation as well as a parameter indicating whether or not fracture deformation affects fracture permeability, as expressed below:

$$\begin{aligned} Fracture\ aperture \\ &= 0.001m \\ &+ average\ fracture\ deformation \times Parameter \end{aligned} \tag{6.3}$$

Table 6-6. Properties of 2-D EGS model

PROPERTY	VALUE	UNIT
Rock mass		
Density	2445	kg/m^3
Porosity	0.19	-
Permeability	8.79×10^{-17}	m^2
Biot coefficient	0.74	-
Heat capacity	723.5	$J/(kg \cdot K)$
Thermal conductivity	3.75	$W/(m \cdot K)$
Initial temperature	373.15	K
Coefficient of thermal expansion	8.60×10^{-6}	K^{-1}
Fracture aperture	0.001	m
Pore fluid		
Density	1000	kg/m^3
Viscosity	1	cP
Heat capacity	4184	$J/(kg \cdot K)$
Thermal conductivity	0.6	$W/(m \cdot K)$
Thermal expansion coefficient	1.98×10^{-4}	K^{-1}
Wellbores		
Diameter	0.01	m

Boundary conditions:

- the four boundaries are impervious to thermal and fluid flow
- the side boundaries are assigned ‘roller:’ displacement normal to the boundaries is zero, mathematically represented as $u \cdot n = 0$
- the top and bottom boundaries are assigned ‘free:’ no constraints or loads acting on the boundaries

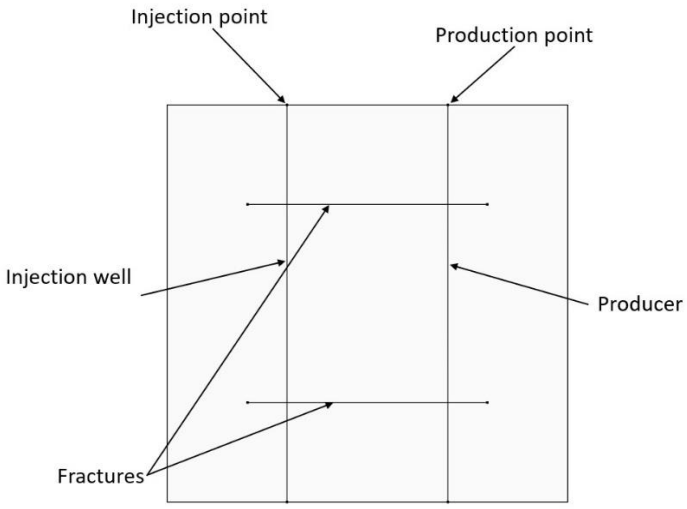

Figure 6-6.Two-dimensional schematic diagram of an EGS with double horizontal fractures completely traversed by two vertical wells, one (left-side) for injection and the other (right-side) for production.

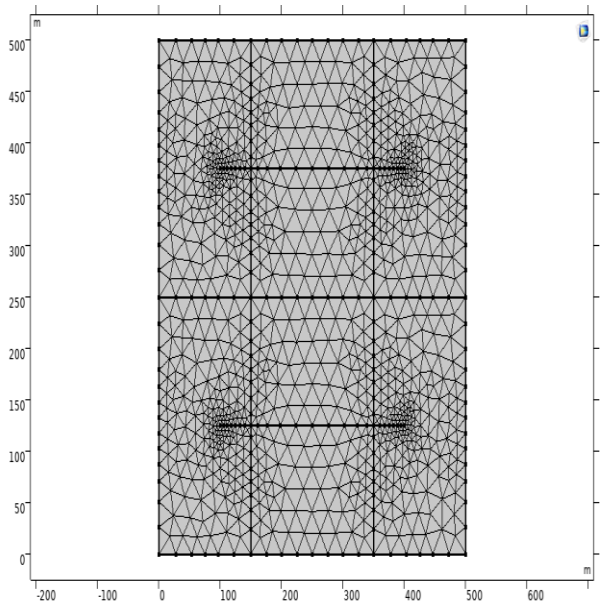

Figure 6-7. An illustration of the domain after a triangular meshing that generated 2116 elements over a mesh (domain) area of $250{,}000.0m^2$.

6.4 A Coupled 3-D Model of a Fractured Geothermal Reservoir

The final model is three-dimensional and a more realistic replica (in thermo-elastic properties) of the 2-D Enhanced Geothermal System model presented in section 6.3 The system is located at 500m depth below the surface and has dimension $500m \times 500m \times 500m$. As shown on Figure 6-8, the two fractures are represented by two rectangular plates, each located at center of the two halves of the domain. At a distance of 250m apart, the fractures are both assigned an aperture of 1cm; the two wells (one injection and the other production) are also positioned equidistant from the boundaries of the domain with wellbore diameter of 1m each. Water is injected at $310.15K$ at a mass flux of $20kg/(m^2 \cdot s)$ For the establishment of a better drainage to maximize production as well as to ensure a more detailed analysis of short-circuiting, the two wells were designed to cross both fractures, completely traversing the reservoir at a depth of 750m below ground level, coinciding with the center of the domain. This set up is carefully planned to essentially create a symmetric scheme that was employed to cut down computational cost by almost 50% as can be seen on Figure 6-8 and Figure 6-10. The four surface boundaries of the reservoir are assigned 'no-flow' condition, and the reservoir is insulated at the outer surfaces. See Table 6-7 for details about the applied mesh and Figure 6-10

showing the half-meshed model due to symmetry. The thermos-hydro-mechanically coupled model was run for 20 years, and the solution was obtained after 97 timesteps with a runtime ranging from 10 minutes to about 2 hours 40 minutes depending on the capacity of the computer used.

Table 6-7. Properties of the applied mesh

MESH PROPERTY	VALUE
Number of tetrahedral elements	29,997
Number of triangular elements	5,934
Number of edge elements	40
Mesh volume	$6.25 \times 10^7 m^3$

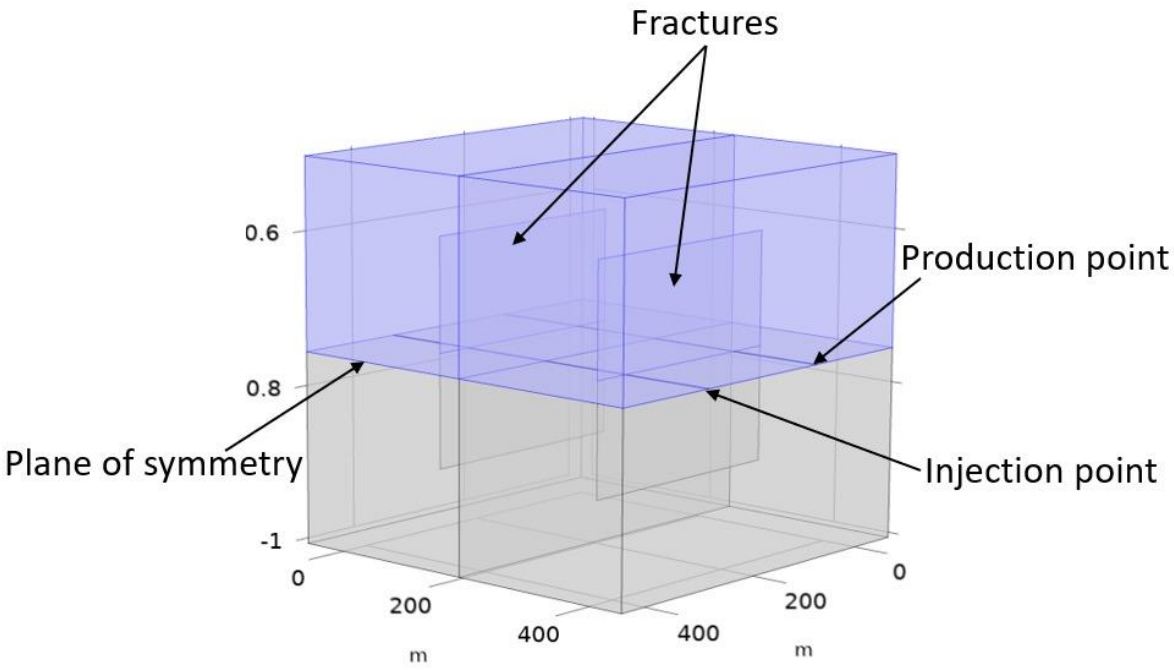

Figure 6-8. A symmetric 3-D model of an EGS with two fractures and two wells.

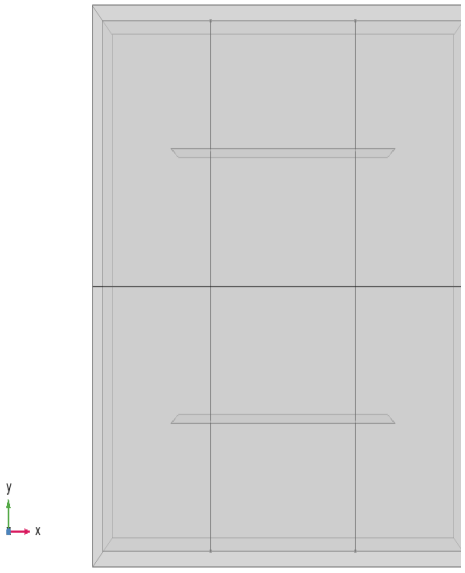

Figure 6-9. A cross-section of the 3-D EGS model showing the two plate-like fractures and the two traversing wells: injection on left-side and production on right-side.

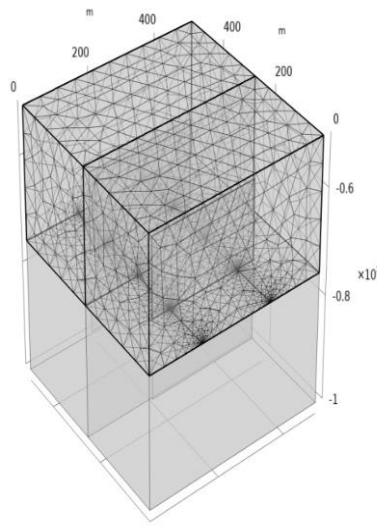

Figure 6-10. A half-meshed 3-D EGS model, which is possible due to the symmetric nature of the model, allowing for a reduced computational effort.

Table 6-8. Property of 3-D EGS model

PROPERTY	VALUE	UNIT
Rock mass		
Density	2445	kg/m^3
Porosity	0.19	-
Permeability	8.79×10^{-7}	m^2
Biot coefficient	1	-
Heat capacity	723.5	$J/(kg \cdot K)$
Thermal conductivity	3.75	$W/(m \cdot K)$
Initial temperature	373.15	K
Thermal expansion coefficient	8.6×10^{-6}	K^{-1}
<u>Pore fluid</u>		
Density	1000	kg/m^3
Viscosity	1	cP
Heat capacity	4184	$J/(kg \cdot K)$
Thermal conductivity	0.6	$W/(m \cdot K)$
Thermal expansion coefficient	1.98×10^{-4}	K^{-1}
<u>Wellbores</u>		
Diameter	0.01	m

CHAPTER 7

RESULTS AND DISCUSSION

7.1 Preliminary Test Results

7.1.1 Thermal strain

Figure 7-1 to Figure 7-12 show the results of the three scenarios. The von Mises stress graph on Figure 7-1 shows evidence of tension, while the temperature and thermal strain graphs together give a reasonable insight: under the mild heating, temperature had increased by only 0.72 thermal strain occurred only at the region where temperature varied. All other contributions of the total strain solely come from the applied tensile axial load. Observe that the thermal strain in this case contributed to about 41% of the total strain.

Similarly, the von Mises stress graph on Figure 7-5 reflects the tension in the specimen as illustrated in scenario 2. It is again observed from the temperature and thermal strain graphs that thermal strain is solely dependent on temperature variation and not external load. The temperature graph (Figure 7-6) shows that the intense heating had almost doubled the overall temperature of the domain after 10 years.

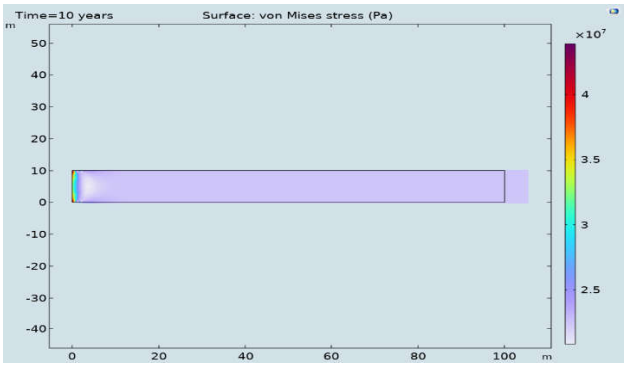

Figure 7-1. Von Mises stress (Scenario 1)

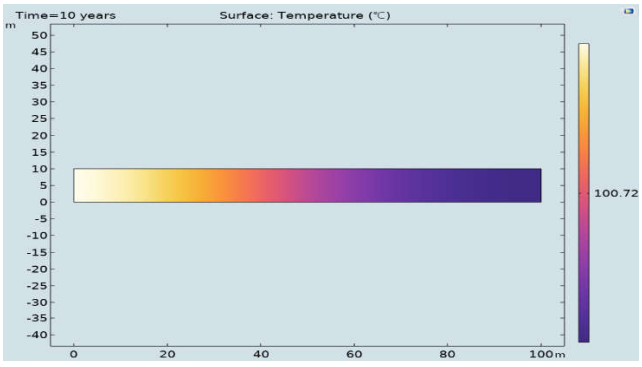

Figure 7-2. Surface temperature (Scenario 1)

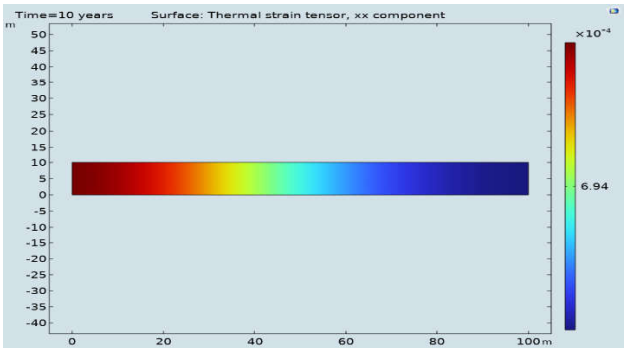

Figure 7-3. Thermal strain (Scenario 1)

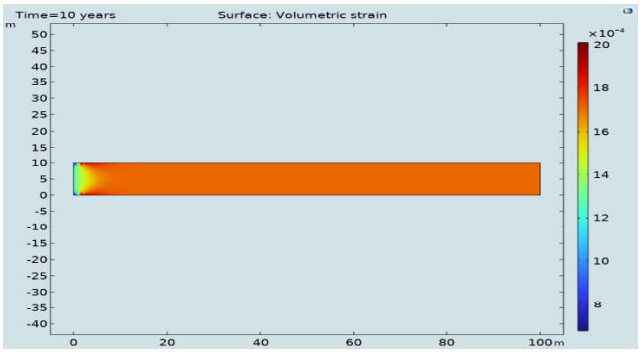

Figure 7-4. Volumetric strain (Scenario 1)

Finally, from Figure 7-11 and Figure 7-12, notice yet another significant contribution of the thermal strain to the total volumetric strain of the specimen. Recall that no external load was applied to scenario 3, and the heated specimen is fixed at both ends; therefore, as seen on the von Mises graph, the specimen could only expand in a direction normal to the fixed boundaries. It is also observed that even though the total thermal strain is tensile, region of increased temperature had lower thermal strain compared to region of decreased temperature.

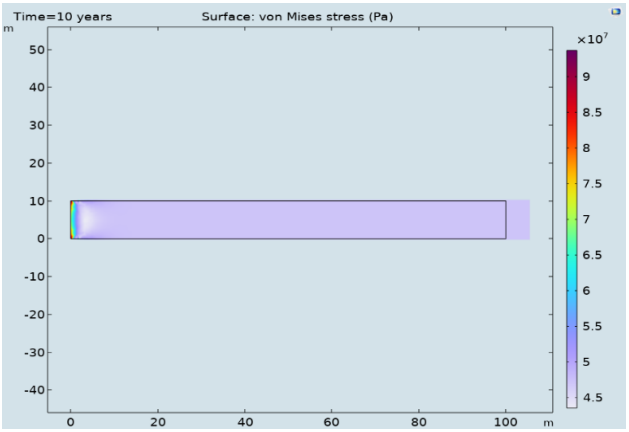

Figure 7-5. Von Mises stress (Scenario 2)

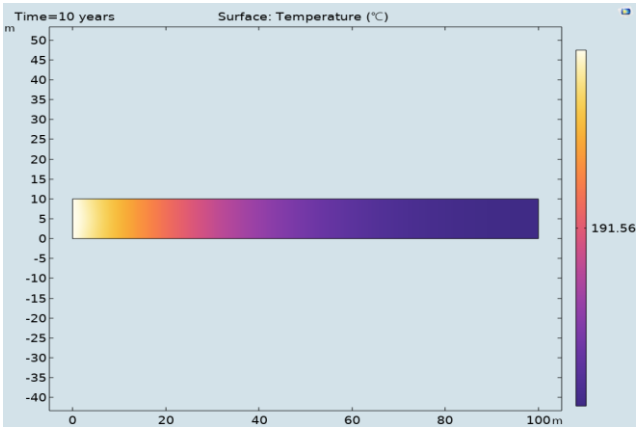

Figure 7-6. Surface temperature (Scenario 2)

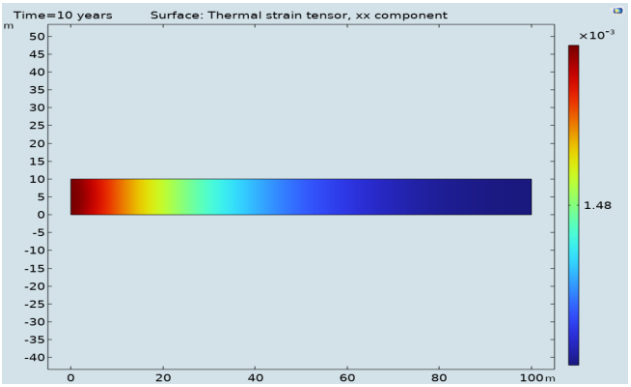

Figure 7-7. Thermal strain (Scenario 2)

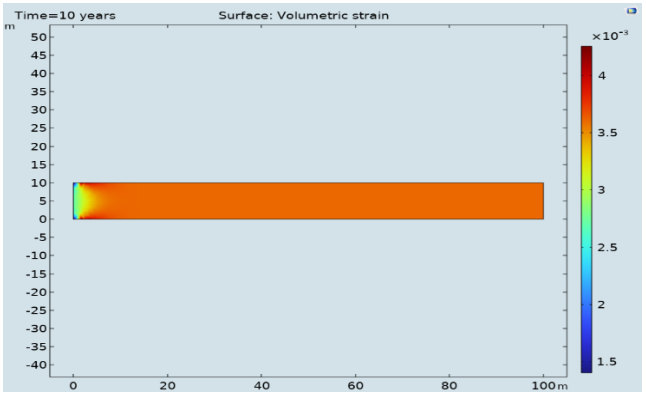

Figure 7-8. Volumetric strain (Scenario 2)

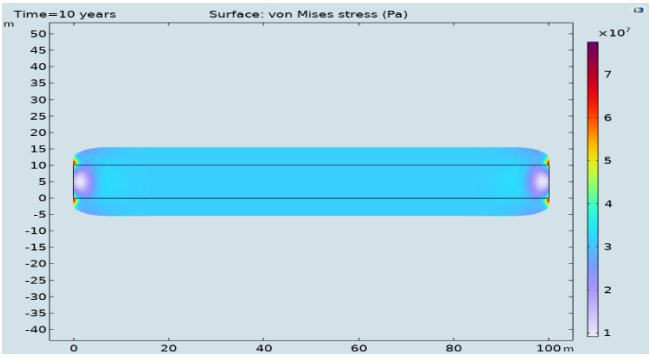

Figure 7-9. Von Mises stress (Scenario 3)

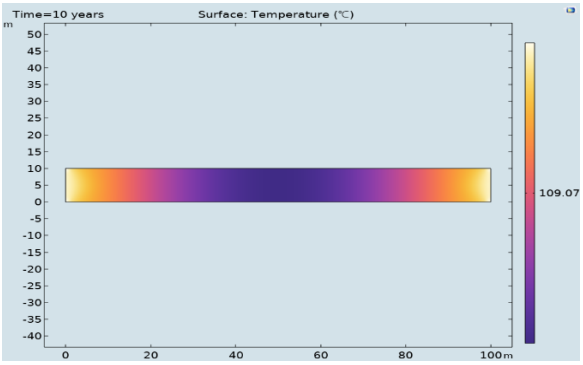

Figure 7-10. Surface temperature (Scenario 3)

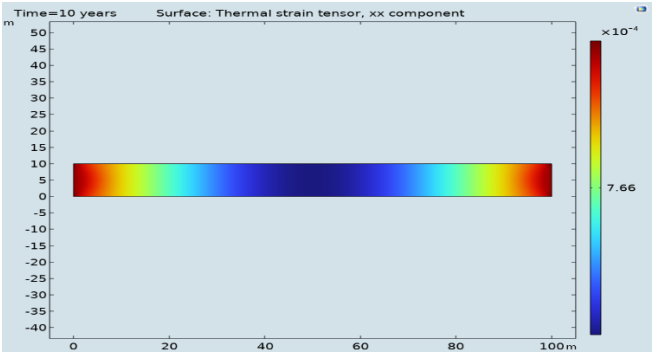

Figure 7-11. Thermal strain (Scenario 3)

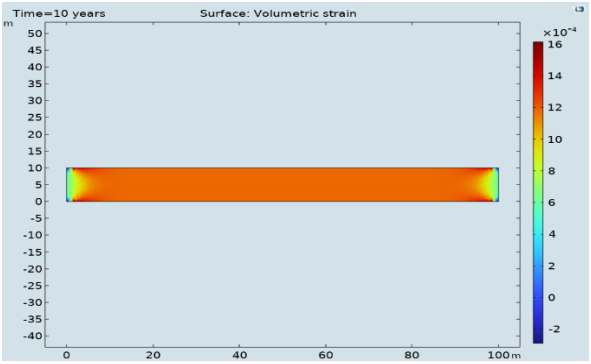

Figure 7-12. Volumetric strain (Scenario 3)

7.1.2 Simplified 3-D Model

'Point Probe 1' is the average pressure along the injection well, while 'Point Probe 2' is the average pressure along the producer. Observe the gradual cooling of the producer with time due to continuous injection of colder working fluid. See Appendix E at APPENDICES for a chronological surface graph showing how the cold working fluid advances within the domain.

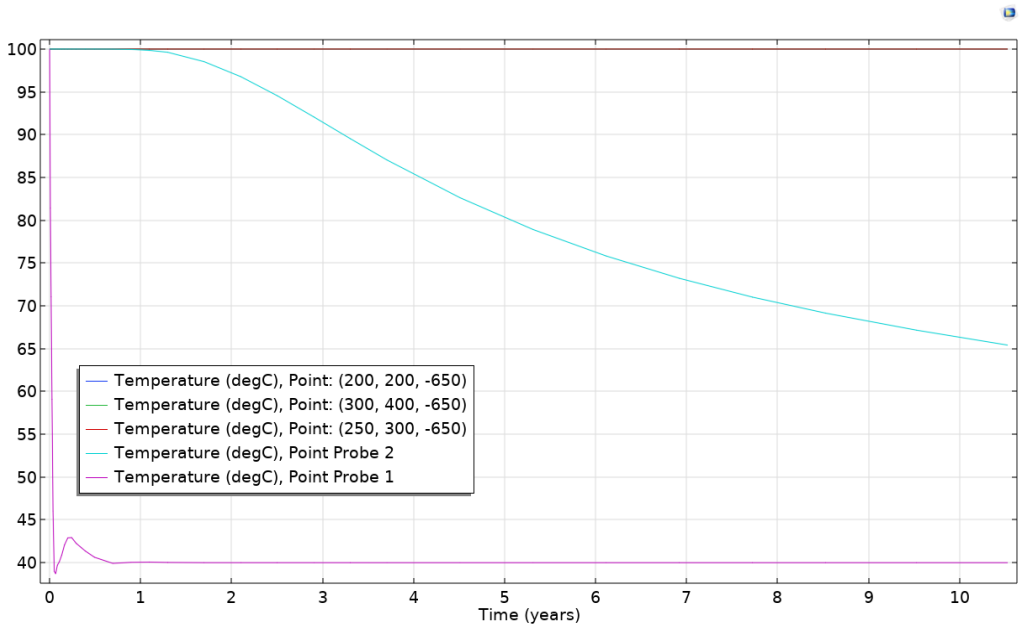

Figure 7-13. Graph of temperature (℃) against time (years) recorded at five selected points within the domain.

7.2 Results of Sample Validation Problems

7.2.1 Terzaghi's 1-D Theorem

As can be observed on Figure 7-14, the generated pore water pressure dissipates in time under the applied load. The current time is 1.5×10^5 $seconds$ (approximately 3 years) since the 0.1MN load was applied, and the pressure along the boundary (y-axis) shows a complete drop (dissipation) from the initial. The pressure profile, after a complete drainage across the top boundary of the medium, would assume initial state. The figure, therefore, further confirms a geomechanical principle that, in the long run, all stresses applied over a porous structure will be taken entirely by matrix. The result shows a fairly compelling agreement with that obtained by (Teichtmeister et al., 2019), which serves to confirm the validity of the model.

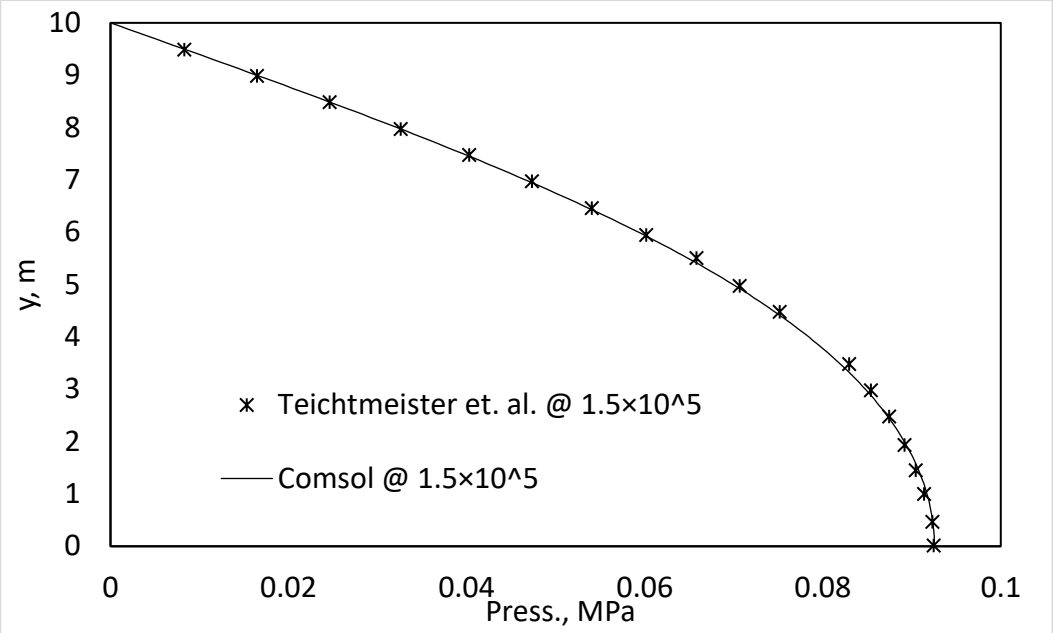

Figure 7-14. A graph showing a solution to Terzaghi's 1D consolidation problem. The ordinate is length (m) along the vertical boundary while the abscissa is pressure in megapascal.

7.2.2 Mandel-Cryer Effect

Next, we closely analyze the Mandel-Cryer Effect. Figure 7-15 shows the results of the model described in sub-section 6.2.2. The area highlighted in blue rectangle on the graph is the region capturing the Mandel-Cryer effect. Notice the non-monotonic pressure response: the pressure initially increases within 45.8 – 4580 seconds, before a continual decrease afterwards. Another important observation is how the pressure increment is advancing toward the center of the reservoir, away from the boundary. This is a perfect example that visualizes (Abousleiman et al., 1996)'s explanation of the Mandel's effect occurring around the center of the domain as discussed in section 2.1. Another keen observation is made at the initial stage along the reservoir boundary: pressure seems to oscillate just close to the boundary as shown at the corner of the blue curve (at 45.8s). This is a perfect reflection of the type and number of elements (or meshed) used in the spatial discretization. A better mesh size tends to reduce the intensity of the oscillation. See Appendix D at APPENDICES to observe how the oscillation was reduced by increasing the number of elements for a better meshing.

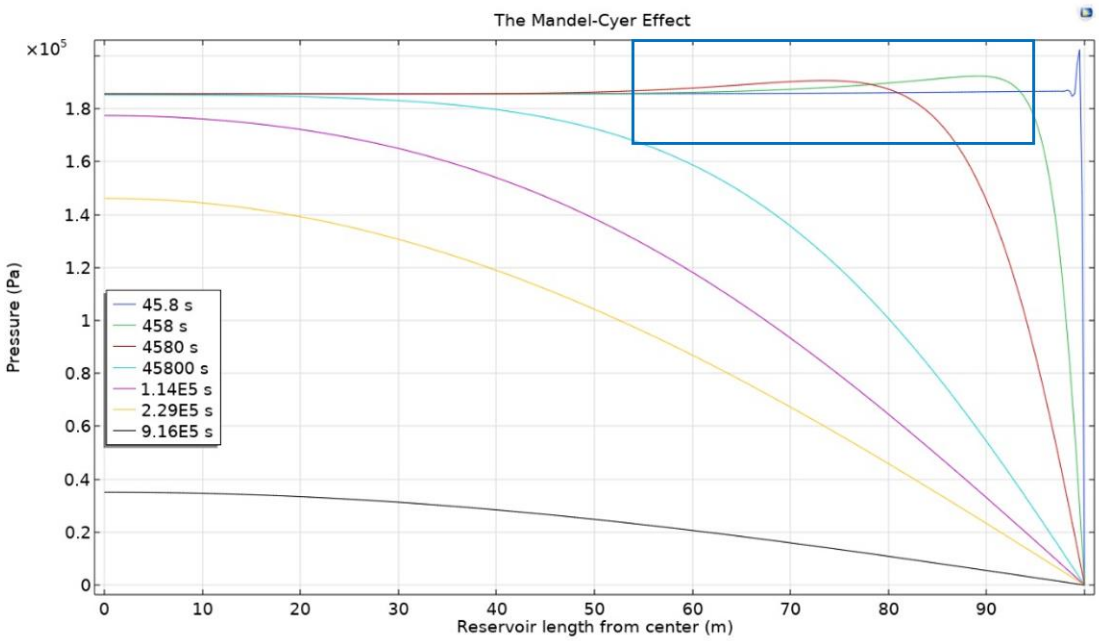

Figure 7-15. Mandel-Cryer Effect captured between 45.8 – 4580 seconds as it advances towards the center of the specimen

7.2.3 Aktan & Ali's Problem

For the last but not least layer of validation, we include the effect of temperature. Figure 7-16 illustrates a graph of pressure versus reservoir depth at four specific times at the center of the medium. We can observe the Mandel-Cryer effect along the day-60 curve: pressure happens to increase relative to the previous times within an interval of about 20m from the left boundary, before dropping along the remaining interval and in subsequent times until the last day (day 160). A thorough explanation of this effect has been made by (Abousleiman et al., 1996): an initial presence of the pore pressure causes extra compressive stiffness of the porous material, which makes the medium become more compliant around the drainage area. The resulting effect is a transfer of a compressive stress towards the stiffer central region, which comes as a mechanism to generate pore pressure, thereby increasing the pressure of the center. Again, we observe an agreement with the results of (Aktan & Ali, 1978), which further bolsters the validity of our model. Figure 7-17 is a chronological illustration of the advancement of the temperature front along the centerline of the reservoir. We observe how by the 100^{th} day the injection temperature had swept almost the entire reservoir, finally breaking through the production well (right boundary) by day 160.

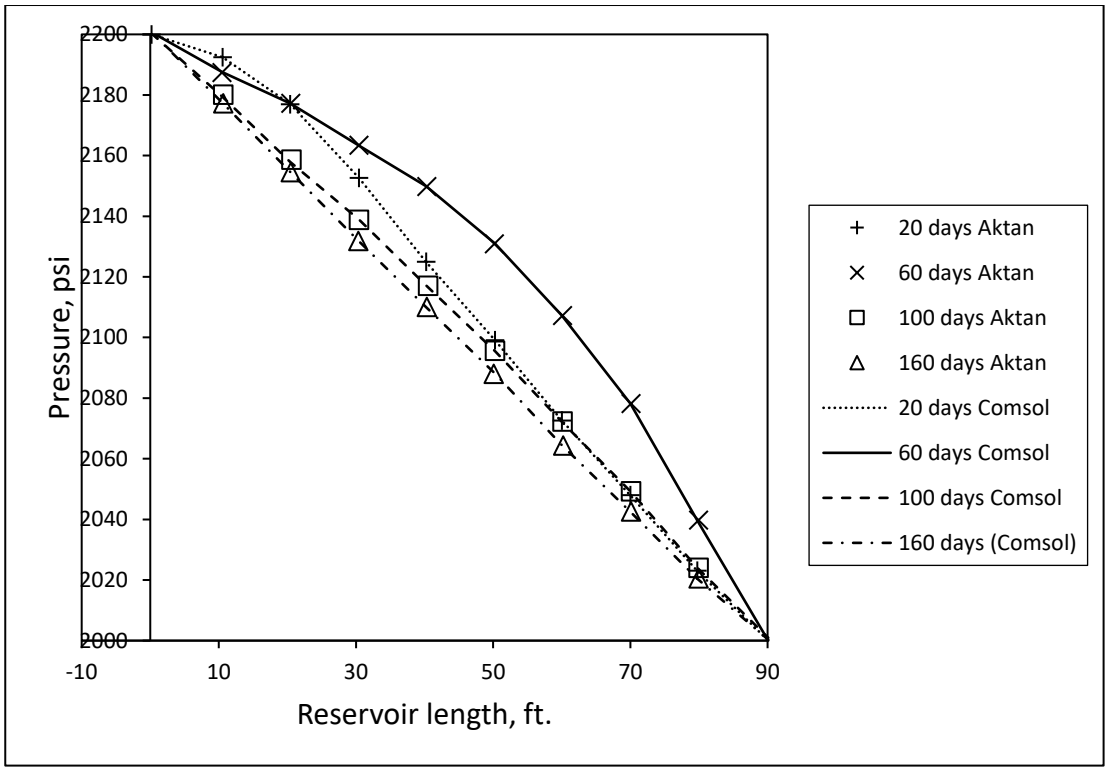

Figure 7-16. A graph of pressure against reservoir length drawn from the centerline of the porous medium. Mandel-Crier effect is observed as 20 and 60-day curves intersect. A perfect match with the results of (Aktan & Ali, 1978) is evident.

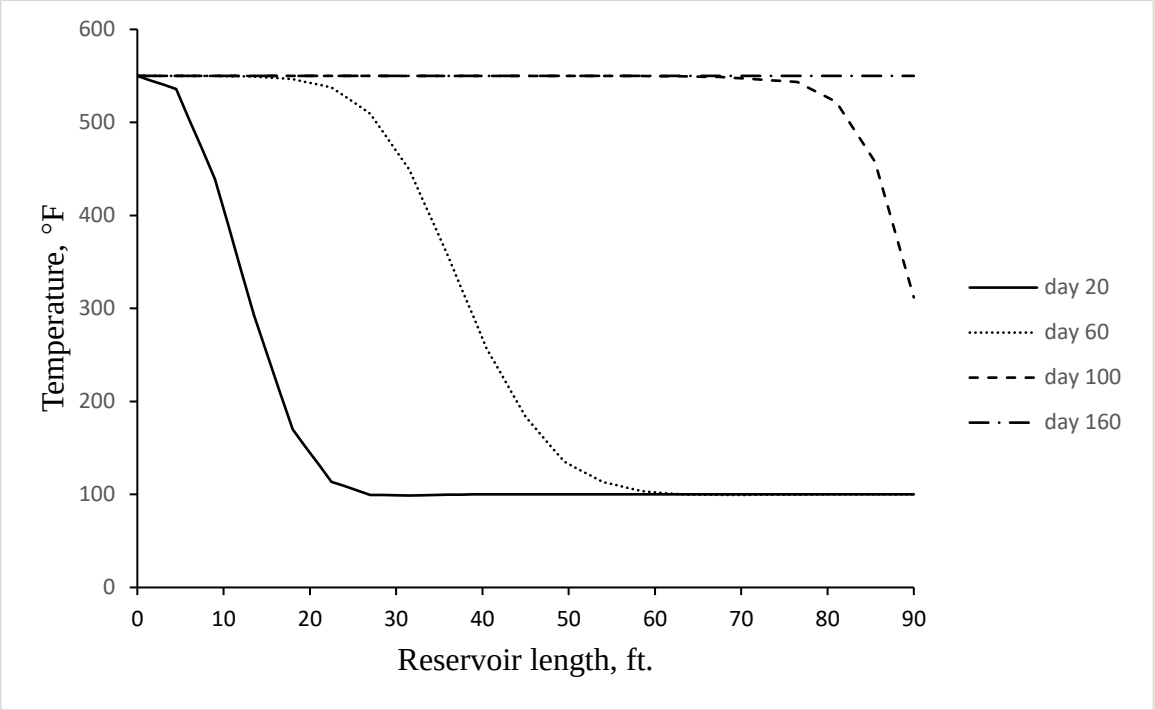

Figure 7-17. Graph of temperature (in deg F) against reservoir length (m)

7.3 2-D Model of a Geothermal Reservoir

Before discussing the results for the coupled 2-D model, it is necessary to give an overview of the various cases considered. First, the results of the three-way coupled model shall be presented, illustrating how 'parametric solution' approach is employed to highlight the effect of fracture deformation on permeability and resulting thermal short-circuiting. Then, sensitivity analysis shall be run to give insights on the parameter that dominates the flow (a comparison between thermal and pressure effects).
The 'parametric solution' feature is denoted by 'parameter' as seen on the graphs

(Figure 7-18 to Figure 7-23) under the following definition:

Parameter = 1: effect of fracture deformation on fracture permeability EXISTS
Parameter = 0: effect of fracture deformation on fracture permeability DOES NOT EXIST

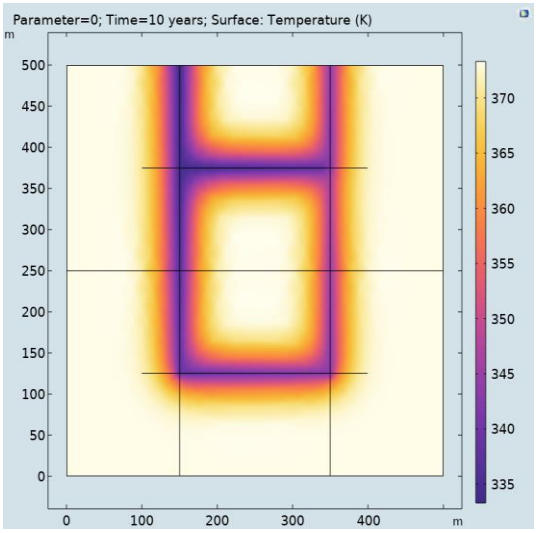

Figure 7-18. Temperature (K) at 10 years when parameter = 0.

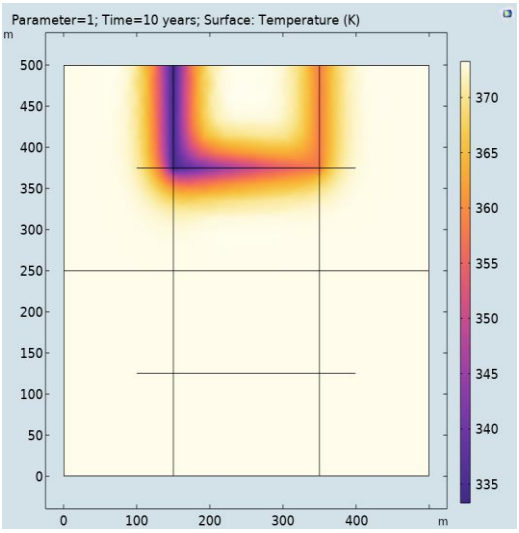

Figure 7-19. Temperature (K)) at 10 years when parameter = 1. Notice the resulting thermal short-circuiting.

By comparing Figure 7-18 and Figure 7-19 above, notice how the injected cold waterfront advances within the reservoir (after a decade) when fracture deformation (which leads to changes in fracture aperture) does not influence permeability (Figure 7-18). Unaffected permeability means both fractures are *always* accessible, even though the top fracture gets a *slight preference* due to its proximity to the injection point, as expected. On Figure 7-19, however, the outcome is quite striking: the water front's preference of the top fracture had grown with time due to the relatively more rapid 'expansion' of its fracture aperture compared to the fracture below. This effect had in the long run caused the working fluid to neglect the latter's flow path as its initial permeability remains unchanged while permeability of the former increases; therefore, the working fluid's preference of the nearer fracture results in thermal short-circuiting (from the injection well, directly through the top fracture, to the

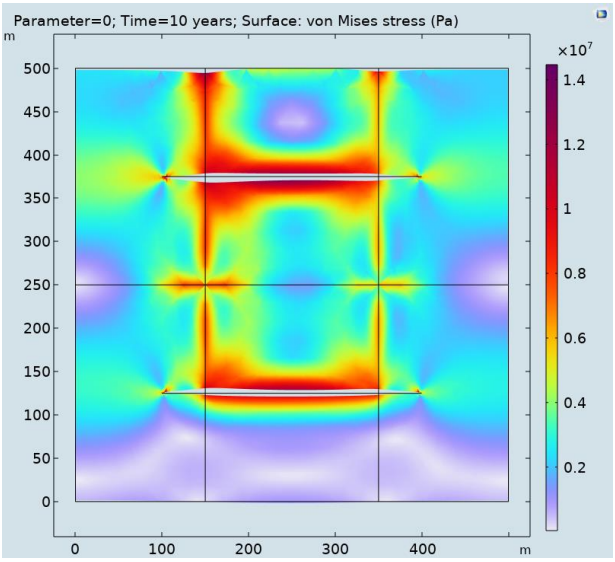

Figure 7-20. Von Mises stress (Pa) with deformation after 10 years when Parameter = 0. Deformation is exaggerated by scale factor of 250.

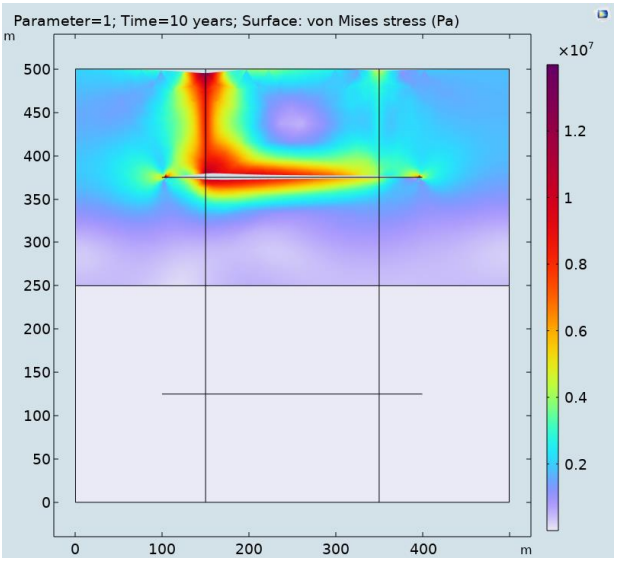

Figure 7-21. Von Mises stress (Pa) with deformation after 10 years when Parameter = 1. Deformation is exaggerated by scale factor of 250.

producer). It should be noted that evidence of thermal short-circuiting, in our case, was only possible because changes in fracture aperture was taken into account; in other words, ignoring the fracture aperture variation bears a consequence of overestimating the system's heat extraction capacity. Another observable effect is that the average reservoir temperature due to fractures' temperature is decreasing at a relatively faster rate when Parameter=0 compared to when Parameter=1, resulting in a relatively 'cooler' domain as seen on Table 7-1. Figure 7-20 and Figure 7-21 give a more physical view of the changes in fracture aperture. They both show von Mises graph integrated with deformation of the domain. Note that the deformation is exaggerated by a factor of 100 for clarity. Observe how when Parameter=0, the apertures of both fractures remain open to allow continuous flow of the cold front, in contrast with when the 'closure' of the lower fracture to flow when Parameter=1. Also notice the relatively higher *thermal stress* generated when parameter=0 as a result of temperature difference between the flow paths and the entire rest of the domain, although a higher local stress down the injection flow line is visible when Parameter=1.

Next, we analyze the mean properties of the domain for the two parameters to have an insight into their effects. As can be observed on Table 7-1, overlooking the effect of fracture deformation on fracture permeability could lead to an overestimation of production by 4.63 kelvins, which is equivalent in energy to $3.46946804 \times 10^{12}$ joules, estimated as follows:

$$q = mc\Delta T = 2170.45\frac{kg}{m^3} \times (500m \times 500m \times 1m) \times 1381\frac{J}{kg \cdot K} \times 4.63K$$

Also observe the overestimation of stress by almost three folds as well as displacement by over 3 folds.

Table 7-1. Mean domain properties for the two parameters

PROPERTY	PARAMETER=0	PARAMETER=1
Temperature, K	366.86	370.82
Stress, MPa	3.08	1.05
Displacement	0.0065572	0.0019807

Finally, sensitivity analyses were conducted for three reservoir properties: Biot's coefficient (α), coefficient of thermal expansion (β, 1/K), and fluid injection rate as mass flux ($Inj, kg/m^2/s$). Note that throughout the sensitivity analyses, all *other* properties of the domain remain unchanged. Table 7-2 shows the results obtained for the mean domain properties (temperature, stress, and displacement) after a sensitivity analysis for Biot's coefficient. Generally, we infer from the table that, for a given parameter, change in Biot's coefficient does not affect temperature, while increasing α leads to decrease in stress and (consequently) decreasing the severity of deformation. Also observe how stress and displacement barely change at Parameter=1 but show conspicuous change at Parameter=0.

Table 7-2. Sensitivity analysis for Biot's coefficient (α)

PROPERTY	PARAMETER=0	PARAMETER=1
Temperature, K for		
$\alpha = 0.64$	366.86	371.07
$\alpha = 0.74$	366.86	371.07
$\alpha = 0.84$	366.86	371.07
Stress, Pa for		
$\alpha = 0.64$	3.0779×10^6	1.0451×10^6
$\alpha = 0.74$	3.0759×10^6	1.0451×10^6
$\alpha = 0.84$	3.0738×10^6	1.0451×10^6
Displacement, m for		
$\alpha = 0.64$	0.0065643	0.0019807
$\alpha = 0.74$	0.0065572	0.0019807
$\alpha = 0.84$	0.0065502	0.0019806

The next sensitivity analysis is conducted for thermal expansion coefficient, ranging from $5.95 \times 10^{-6}\ K^{-1}$ to $1.128 \times 10^{-6}\ K^{-1}$. The intermediate values differ by a constant, except for $\beta = 8.60 \times 10^{-6}$, which is the value for our original model. A

close observation on Table 7-2 and Table 7-3 shows that coefficient of thermal expansion has more effect on stresses and strains compared to the Biot's coefficient.

Table 7-3. Sensitivity analysis for coefficient of thermal expansion (β, K^{-1})

PROPERTY	PARAMETER=0	PARAMETER=1
Temperature, K for		
$\beta = 5.95 \times 10^{-6}$	366.86	370.89
$\beta = 7.73 \times 10^{-6}$	366.86	371.02
$\beta = 8.60 \times 10^{-6}$	366.86	371.07
$\beta = 9.50 \times 10^{-6}$	366.86	371.12
$\beta = 1.13 \times 10^{-5}$	366.86	371.21
Stress, Pa for		
$\beta = 5.95 \times 10^{-6}$	2.1230×10^{6}	7.7880×10^{5}
$\beta = 7.73 \times 10^{-6}$	2.7631×10^{6}	9.6080×10^{5}
$\beta = 8.60 \times 10^{-6}$	3.0759×10^{6}	1.0450×10^{6}
$\beta = 9.50 \times 10^{-6}$	3.3995×10^{6}	1.1303×10^{6}
$\beta = 1.13 \times 10^{-5}$	4.0496×10^{6}	1.2950×10^{6}
Displacement, m for		
$\beta = 5.95 \times 10^{-6}$	0.0045205	0.0014184
$\beta = 7.73 \times 10^{-6}$	0.0058886	0.0017970
$\beta = 8.60 \times 10^{-6}$	0.0065572	0.0019807
$\beta = 9.50 \times 10^{-6}$	0.0072492	0.0021697
$\beta = 1.13 \times 10^{-5}$	0.0086330	0.0025458

Table 7-4. Sensitivity analysis for injection rate as mass flux (Inj, $kg/m^2/s$)

PROPERTY	PARAMETER=0	PARAMETER=1
Temperature, K for		
$Inj = 5$	369.96	371.75
$Inj = 10$	368.42	371.32
$Inj = 20$	366.86	370.89
$Inj = 30$	366.30	370.66
$Inj = 40$	366.00	370.68
Stress, Pa for		
$Inj = 5$	1.1514×10^{6}	5.1505×10^{5}
$Inj = 10$	1.6956×10^{6}	6.4381×10^{5}
$Inj = 20$	2.1230×10^{6}	7.7880×10^{5}
$Inj = 30$	2.2900×10^{6}	7.5278×10^{5}
$Inj = 40$	2.3754×10^{6}	9.0055×10^{5}
Displacement, m for		

$Inj = 5$	0.0025956	0.0011620
$Inj = 10$	0.0036655	0.0012991
$Inj = 20$	0.0045205	0.0014184
$Inj = 30$	0.0048700	0.0014886
$Inj = 40$	0.0050532	0.0015395

7.4 3-D Model of a fractured Geothermal Reservoir

Recall that this 3-D model is an augmented form of the 2-D model discussed in the previous sub-section. The results of the model, therefore, provide a more realistic view of the concept of thermal short-circuiting. Figure 7-22 shows the result after 20 years when Parameter is 0 (see sub-section 8.2). Notice how the cold front continues to flow through both fractures when fracture aperture has no impact on fracture permeability. Figure 7-23, however, shows evidence of thermal short-circuiting after 20 years, owing to the effect of increasing fracture aperture on fracture permeability.

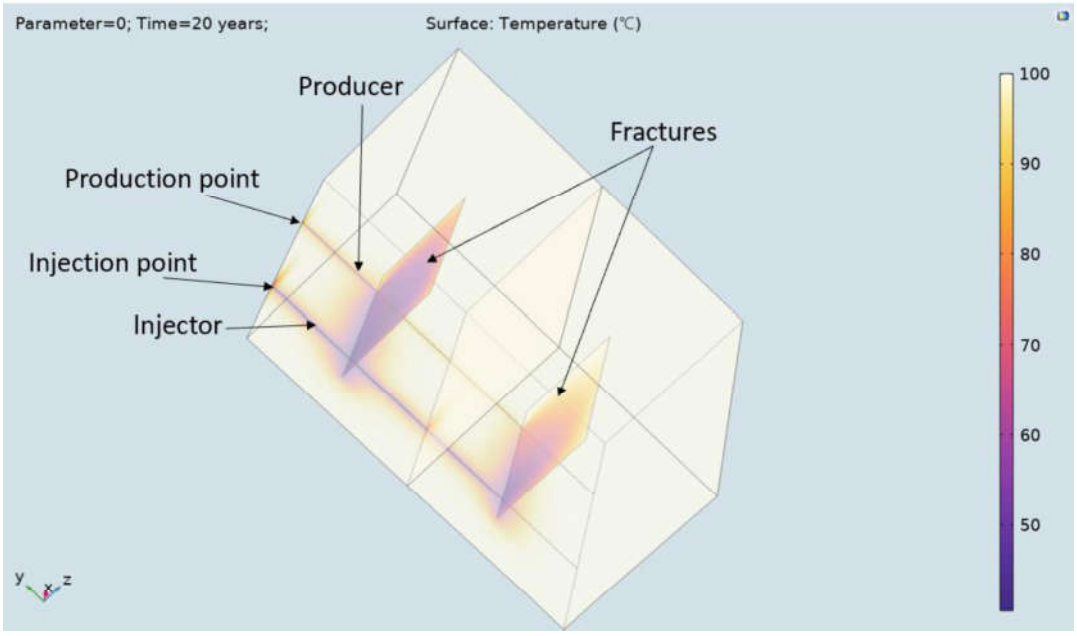

Figure 7-22. Temperature (°C) at 20 years when Parameter=0. Both fractures remain accessible since fracture deformation does not affect fracture permeability.

As the cold working fluid continues to prefer the nearer fracture, its transmissivity increases in a more rapid manner compared to the farther fracture; hence, the latter tends 'show' more resistance to flow, causing it to be completely neglected eventually. Figure 7-24 and Figure 7-25 show surface temperature of the two parametric conditions at the plane of symmetry, reflecting almost the same results as in the 2-D case presented in the previous section. Note that this view by the plane

parametric conditions at the plane of symmetry, reflecting almost the same results as in the 2-D case presented in the previous section. Note that this view by the plane of symmetry does not capture the state of the fractures, as both fractures are oriented

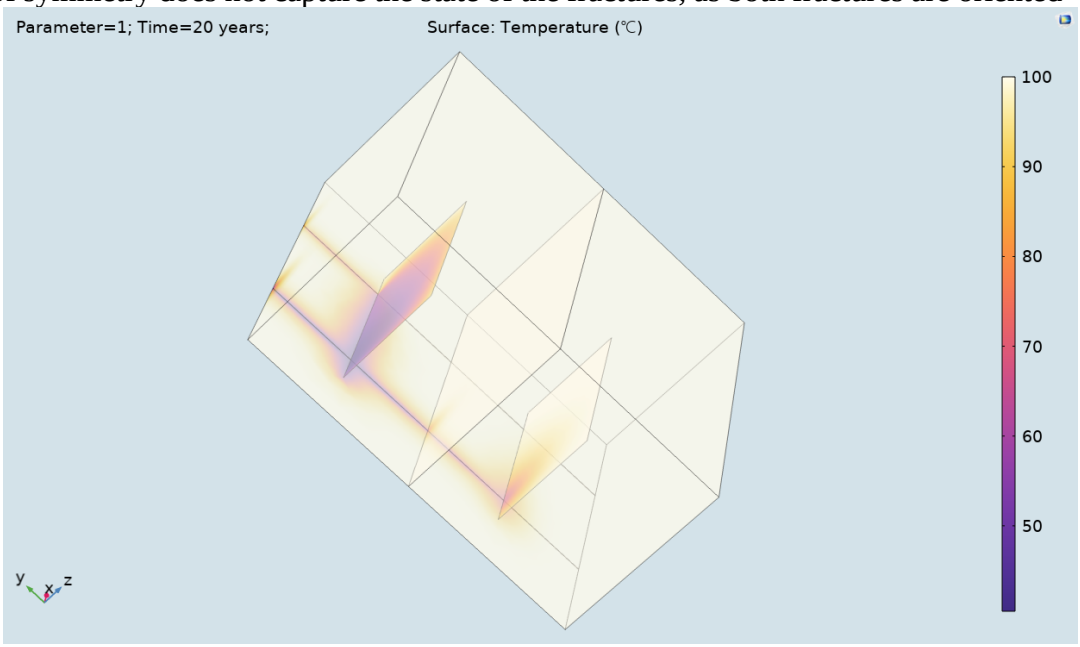

Figure 7-23. Temperature (℃) at 20 years when Parameter=1. Thermal short-circuiting occurs as the cold front prefers fracture nearer to the injection point, increasing fracture aperture in the long run while decreasing that of the farther fracture until a complete shutdown.

normal to that plane. Both the 2-D and 3-D models are therefore underscoring the significant impact of fracture aperture variation on the fracture's transmissivity. These observations further highlight the importance of coupling thermo-poroelasticity in geothermal systems. The rock matrix, no matter how seemingly rigid, retains its tendency to expand or contract under the influence of pressure and/ or temperature, and because it is quite challenging to determine the exact contribution of each of the two to the rock's expansion (or contraction), it is consequential to ignore the effect of any, especially that of temperature, in geothermal systems.

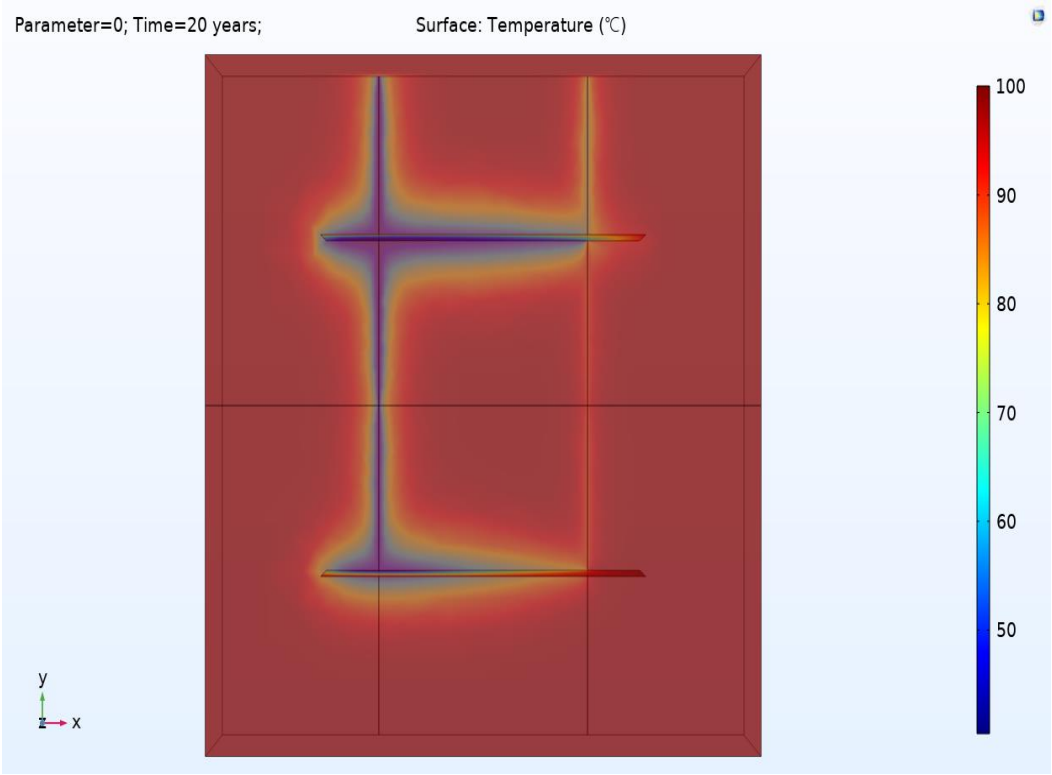

Figure 7-24. Surface temperature (now in ℃) at 20 years when Parameter = 0, at the plane of symmetry (located at a depth of 750m). Recall similar results obtained from the 2-D model.

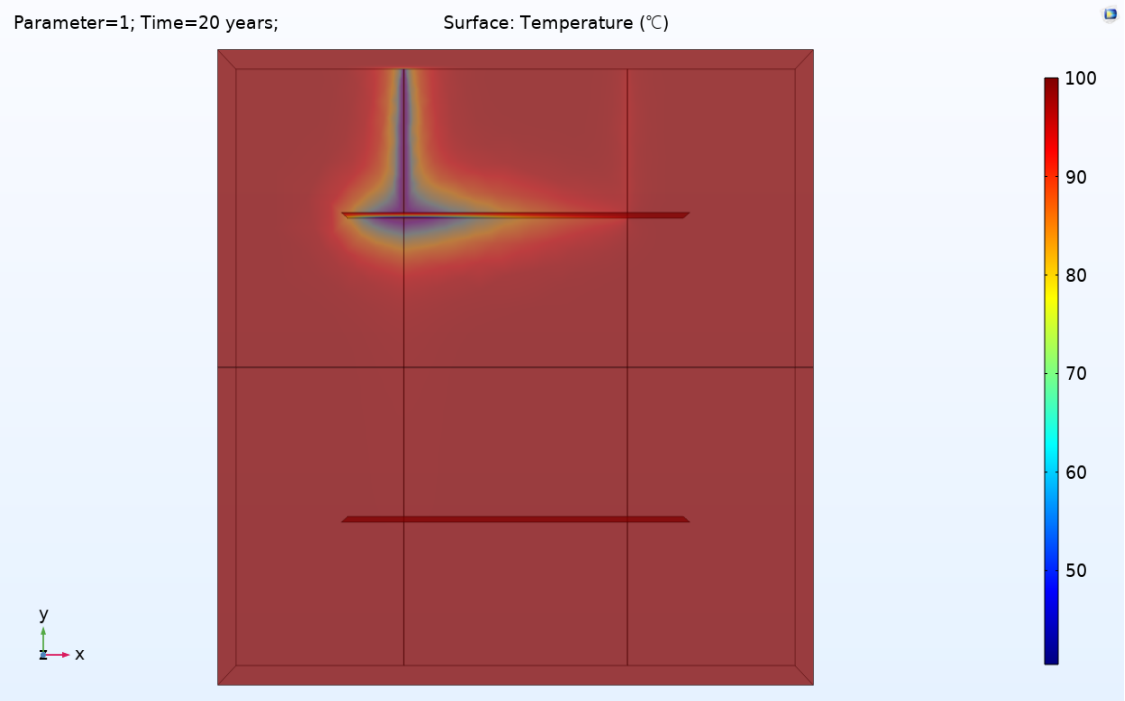

Figure 7-25. Surface temperature (in ℃) at 20 years when Parameter = 1, at the plane of symmetry revealing evidence of thermal short-circuiting.

CHAPTER 8

CONCLUSION

The three fundamental balance equations, namely, mass balance, momentum balance and energy balance equations were derived for coupled numerical modelling of a geothermal reservoir. These equations, constituting the thermo-poroelastic behavior evident in subsurface formations, were solved in a coupled way to mimic the reality, as porosity and permeability (including fracture aperture) are affected by not only changes in stress but also temperature. The poroelastic part of the model was tested for validation using both Terzaghi's 1-D consolidation problem and the more recent Mandel's problem, reconfirming the existing Mandel-Cryer effect. Results of our models for both the former and latter were compared with those obtained by (Teichtmeister et al., 2019), and a substantial agreement prevailed between the two results. The sudden initial pressure build-up and its slow dissipation across the drainage boundaries were observed in both cases. However, the Mandel-Cryer model showed the continuous increase in pressure at regions away from the boundary, before a later dissipation was observed. For validating the thermo-poroelastic model, Aktan and Farouk's model was employed. In all cases, a perfect match is observed between our results and those of the aforementioned works (i.e. Terzaghi, Mandel-Cryer and Aktan & Farouq). Finally, a typical Enhanced Geothermal System was modelled to analyze the effect of temperature on fracture aperture and the resulting short-circuiting. Close analyses of the related thermo-poroelastic models reveal the significant impact of change in fracture aperture on the overall productivity of the reservoir. In other words, ignoring the inherent fracture aperture changes tends to overestimate the heat extraction capacity of the reservoir.

Finally, as a possible expansion of this study, further studies could be conducted to examine the failure criteria of the presented models; an even more comprehensive model may model fracture propagation as the yield stresses are locally exceeded.

REFERENCES

Abousleiman, Y., Cheng, A. H.-D., Cui, L., Detournay, E., & Roegiers, J.-C. (1996). Mandel's problem revisited. *Géotechnique*, *46*(2), 187–195. https://doi.org/10.1680/geot.1996.46.2.187

Aktan, T., & Ali, S. M. F. (1978). Finite-Element Analysis of Temperature and Thermal Stresses Induced by Hot Water Injection. *Society of Petroleum Engineers Journal*, *18*(06), 457–469. https://doi.org/10.2118/5765-PA

Bear, J. (1988). *Dynamics of Fluids in Porous Media. Dover Civil and Mechanical Engineering*. Dover Publications.

Beck, M. (2019). *Conceptual approaches for the analysis of coupled hydraulic and geomechanical processes*. Stuttgart University.

Coussy, O. (2004). *Poromechanics* (2. ed). Wiley.

Cryer, C. W. (1963). A Comparison of the Three-dimensional Consolidation Theories of Biot and Terzaghi. *The Quarterly Journal of Mechanics and Applied Mathematics*, *16*(4), 401–412. https://doi.org/10.1093/qjmam/16.4.401

Detournay, E. & Alexander H.-D., Cheng. (1993). Fundamentals of Poroelasticity. *Pergamon Press*.

García-Noval, C., Álvarez, R., García-Cortés, S., García, C., Alberquilla, F., & Ordóñez, A. (2024). Definition of a thermal conductivity map for

geothermal purposes. *Geothermal Energy*, *12*(1), 17. https://doi.org/10.1186/s40517-024-00292-8

Han, G., & Dusseault, M. B. (2003). Description of fluid flow around a wellbore with stress-dependent porosity and permeability. *Journal of Petroleum Science and Engineering*, *40*(1–2), 1–16. https://doi.org/10.1016/S0920-4105(03)00047-0

Huttrer, G. (2020). *Geothermal Power Generation in the World 2015-2020 Update Report*.

International Energy Agency (IEA). (2023). *World Energy Outlook 2023*. International Energy Agency (IEA). https://www.iea.org/reports/world-energy-outlook-2023

IRENA and CPI. (2023). *Global landscape of renewable energy finance, 2023*. International Renewable Energy Agency. https://www.irena.org/Publications/2023/Feb/Global-landscape-of-renewable-energy-finance-2023

Jon Jincai Zhan. (2020). *Applied Petroleum Geomechanics.* Elsevier Inc.

Mandel, J. (1953, June). *Consolidation of Soils (Mathematical Study)*.

Maurice A. Biot. (1941). *General Theory Of Three-dimensional Consolidation*.

Maurice A. Biot. (1955). *Theory of Elasticity and Consolidation for a Porous Anisotropic Solid*.

Maurice A. Biot. (1956). *General Solutions of the Equations of Elasticity and Consolidation for a Porous Material*.

McLean, M. L., & Espinoza, D. N. (2023). Thermal destressing: Implications for short-circuiting in enhanced geothermal systems. *Renewable Energy*, *202*, 736–755. https://doi.org/10.1016/j.renene.2022.11.102

Michael J. Heap et al. (2020). The Thermal Properties of Porous Andesite. *ELSEVIER*, 13.

Paul A. Siratovich, Michael J. Heap, Marlene C. Villenueve, James W. Cole, & Thierry Reuschle. (2014). Physical Property Relationships of the Rotokawa Andesite, a Significant Geothermal Reservoir Rock in the Taupo Volcanic Zone, New Zealand. *Geothermal Energy*, 31.

Siratovich, P. A., Von Aulock, F. W., Lavallée, Y., Cole, J. W., Kennedy, B. M., & Villeneuve, M. C. (2015). Thermoelastic properties of the Rotokawa Andesite: A geothermal reservoir constraint. *Journal of Volcanology and Geothermal Research*, *301*, 1–13. https://doi.org/10.1016/j.jvolgeores.2015.05.003

Stacey, F. D., & Loper, D. E. (1988). Thermal history of the Earth: A corollary concerning non-linear mantle rheology. *Physics of the Earth and Planetary Interiors*, *53*(1–2), 167–174. https://doi.org/10.1016/0031-9201(88)90139-2

Suárez-Arriaga, M. C. (2010). *Thermo-poroelasticity in geothermics, formulated in four dimensions*. *23*.

Teichtmeister, S., Mauthe, S., & Miehe, C. (2019). Aspects of finite element formulations for the coupled problem of poroelasticity based on a canonical minimization principle. *Computational Mechanics*, *64*(3), 685–716. https://doi.org/10.1007/s00466-019-01677-4

W. Tester and M. C. Smith. (1977). *Energy Extraction Characteristics of Hot Dry Rock Geothermal Systems*. Twelfth Intersociety Energy Conversion Engineering Conference.

Yang, Y., Cao, Q., Fang, C., & Zhu, C. (2023). Characteristics of geothermal field and evaluation of geothermal resource potential in the Yingjiang Basin. *Energy Geoscience*, *4*(4), 100210. https://doi.org/10.1016/j.engeos.2023.100210

APPENDICES

A. Sensitivity Analysis of Biot's Coefficient (α) at Parameter = 0 and 1

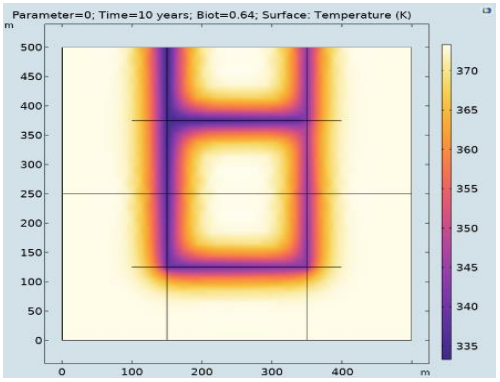

Figure 10-1. Temperature for α=0.64

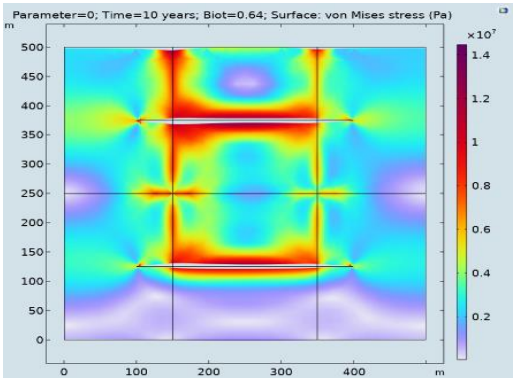

Figure 10-2. Stress for α=0.64

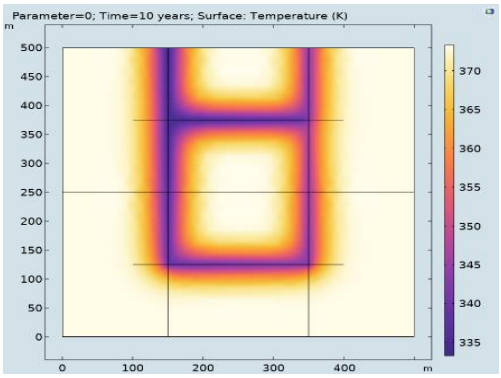

Figure 10-3. Temperature for α=0.74

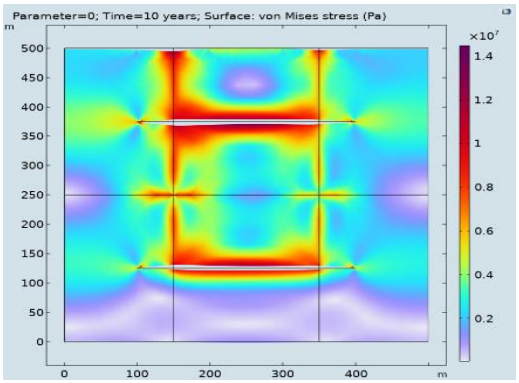

Figure 10-4. Stress for α=0.74

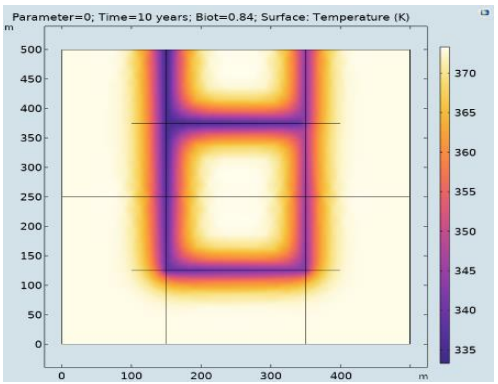

Figure 10-5. Temperature for α=0.84

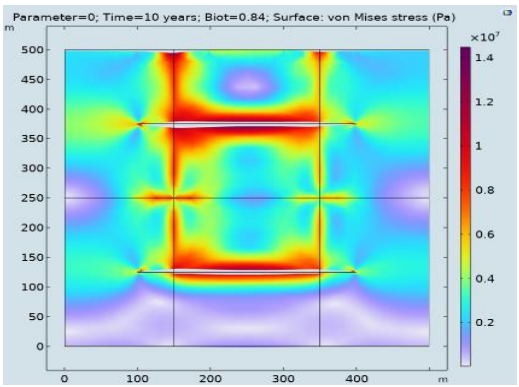

Figure 10-6. Stress for α=0.84

Note that for the sensitivity analyses, as can be seen on the graphs' titles, Figure 10-1 to Figure 10-6 are obtained for Parameter=0, whiles those of Figure 10-7 to Figure 10-12 are obtained for Parameter=1. Notice from the graphs that the surface graphs do not clearly show the disparities of the different Biot's coefficient values used. The tables provided in section 7, therefore, give more elaborate illustrations of the property and parametric nuances. The ambiguity of the surface graphs could be avoided if we are to exaggerate the visuals by, say, a magnitude of several thousands; however, we keep the graphs at this scale to save space.

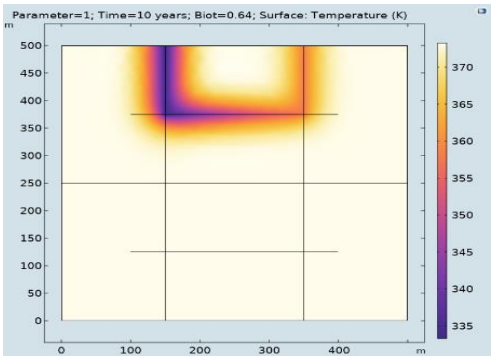

Figure 10-7. Temperature for α=0.64

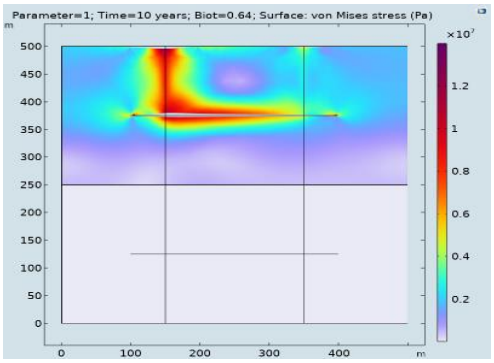

Figure 10-8. Stress for α=0.64

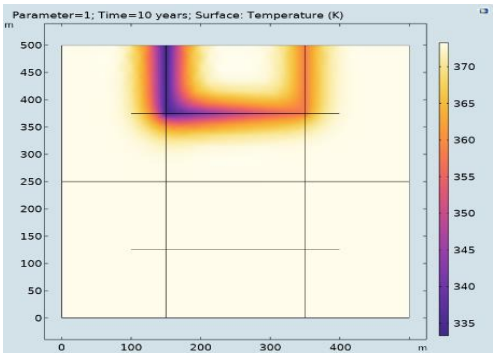

Figure 10-9. Temperature for α=0.74

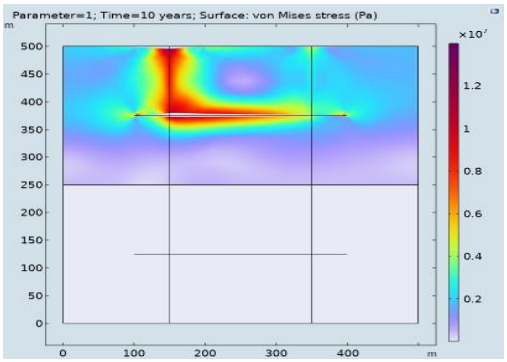

Figure 10-10. Stress for α=0.74

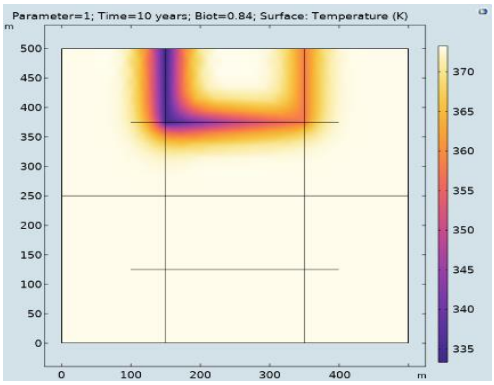

Figure 10-11. Temperature for α=0.84

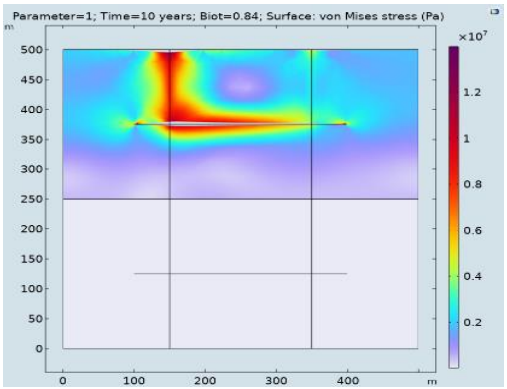

Figure 10-12. Stress for α=0.84

B. Sensitivity Analysis of Coefficient of Thermal Expansion (β, 1/K)

Next, we present sensitivity analysis on some parameters (specifically, coefficient of thermal expansion and injection rate) along the *two fractures* of the 2D model using linear graphs, which tend to be much more illustrative compared to the surface graphs. For each property, we first present the sensitivity with Parameter=0, and then follow that by the corresponding sensitivity for Parameter=1. Each column hereafter shows sensitivity of the property in question to Temperature, Stress and Displacement in order. We begin with sensitivity of β in this appendix; the next appendix (Appendix C) conducts sensitivity for injection rate. Recall from Table 7-3 in Chapter 7 that coefficient of thermal expansion had a positive correlation with stress and displacement, which can be visualized on the stress and displacement graphs in this appendix. Also, temperature graphs reflect the little effect of β on the overall temperature of the domain, as observed earlier in chapter 7.

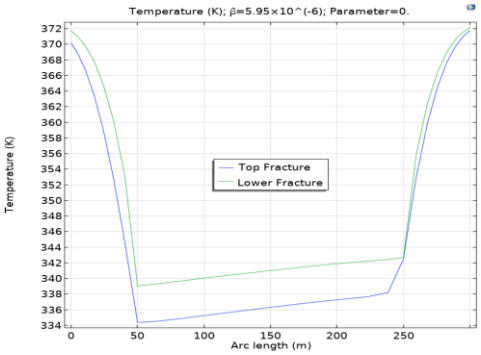

Figure 10-13 Temp. for $\beta = 5.95 \times 10^{-6}$

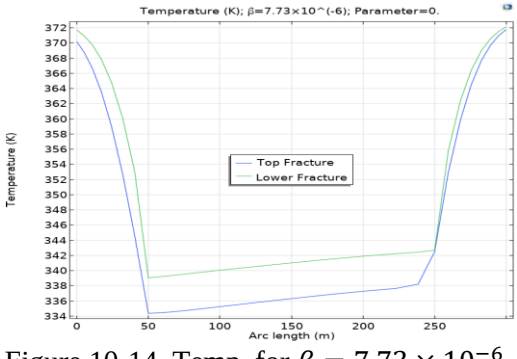

Figure 10-14. Temp. for $\beta = 7.73 \times 10^{-6}$

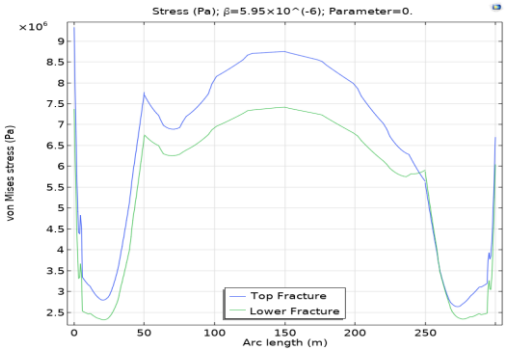

Figure 10-15. Stress for $\beta = 5.95 \times 10^{-6}$

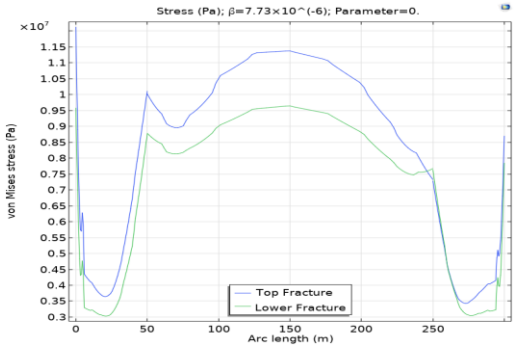

Figure 10-16. Stress for $\beta = 7.73 \times 10^{-6}$

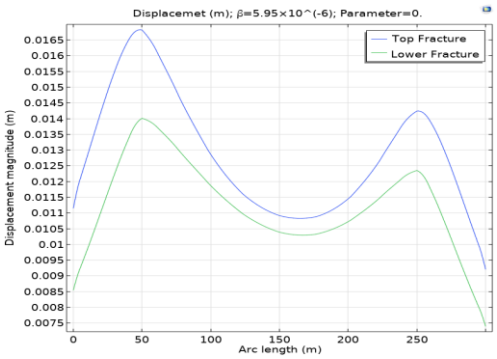

Figure 10-17 Disp. for $\beta = 5.95 \times 10^{-6}$

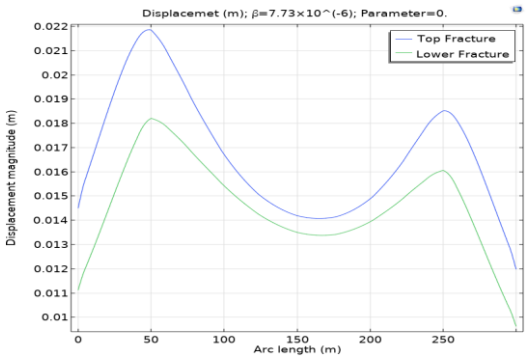

Figure 10-18 Disp. for $\beta = 7.73 \times 10^{-6}$

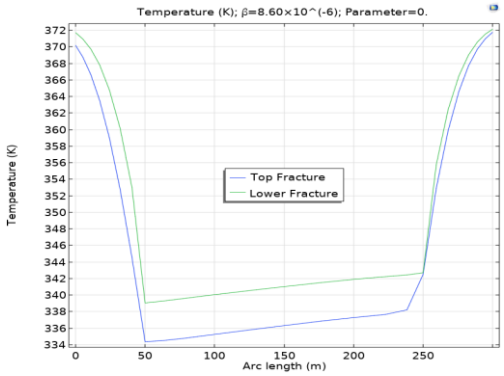

Figure 10-19 Temp. for $\beta = 8.60 \times 10^{-6}$

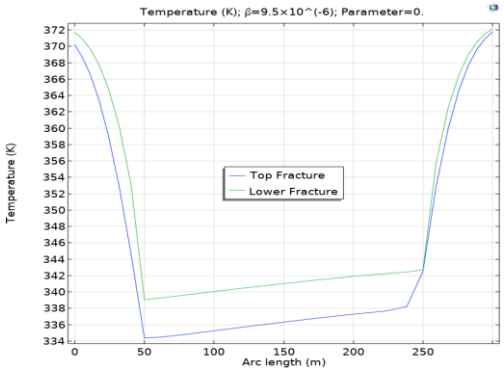

Figure 10-20. Temp. for $\beta = 9.5 \times 10^{-6}$

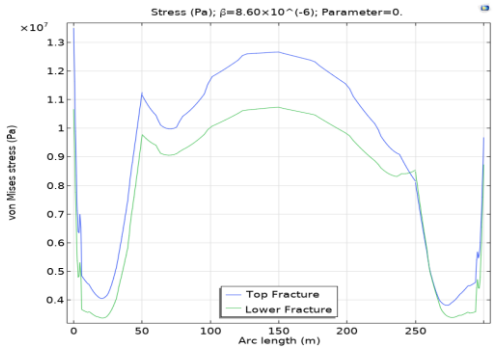

Figure 10-21. Stress for $\beta = 8.60 \times 10^{-6}$

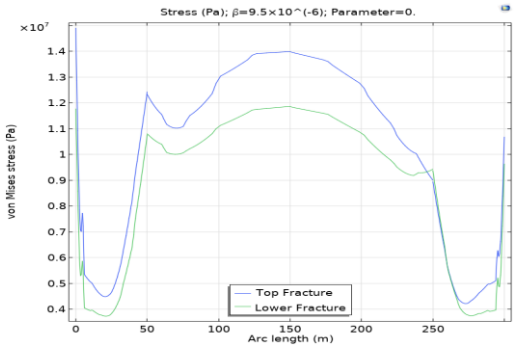

Figure 10-22. Stress for $\beta = 9.5 \times 10^{-6}$

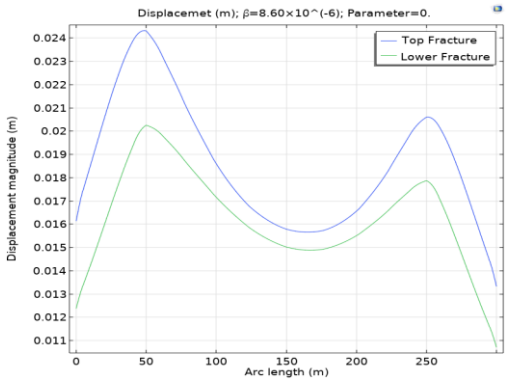

Figure 10-23 Disp. for $\beta = 8.60 \times 10^{-6}$

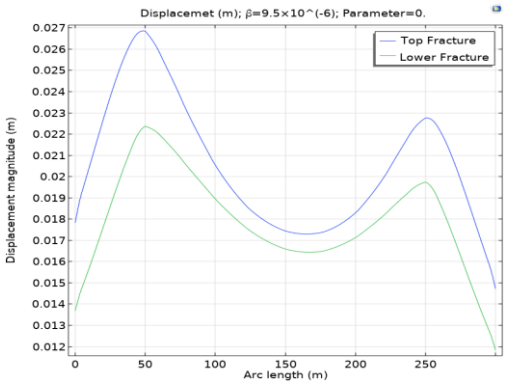

Figure 10-24 Disp. for $\beta = 9.5 \times 10^{-6}$

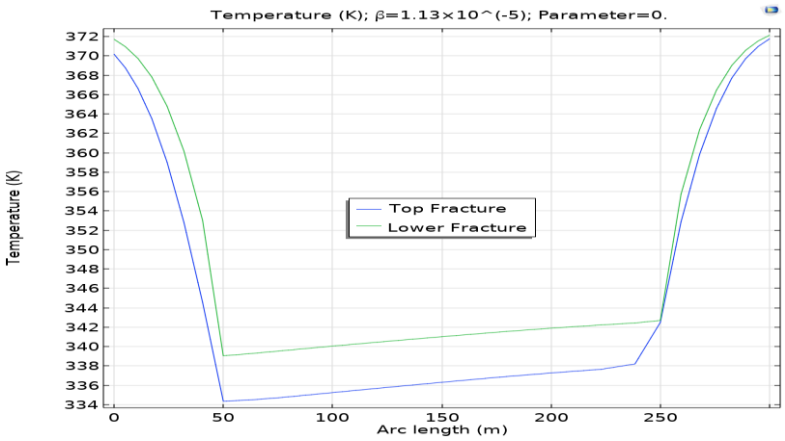

Figure 10-25 Temp: $\beta = 1.13 \times 10^{-5}$

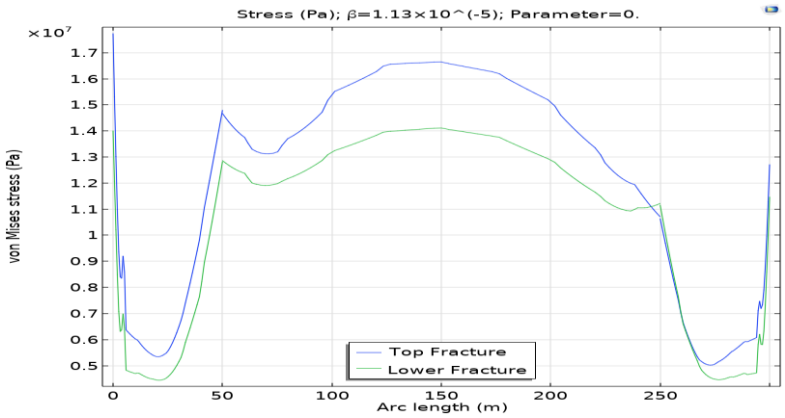

Figure 10-26 Stress: $\beta = 1.13 \times 10^{-5}$

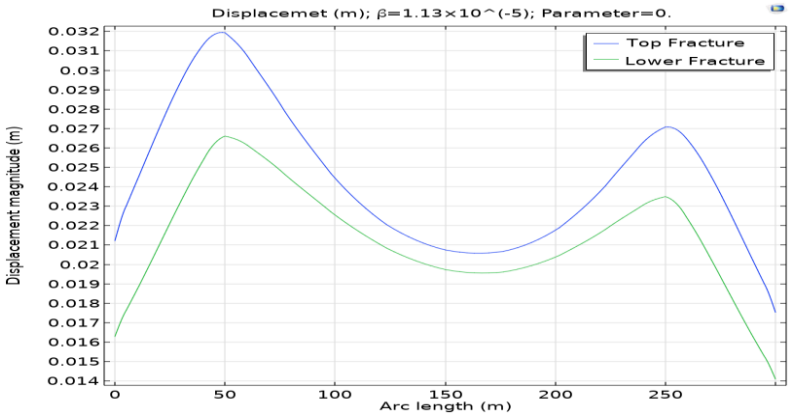

Figure 10-27: $\beta = 1.13 \times 10^{-5}$

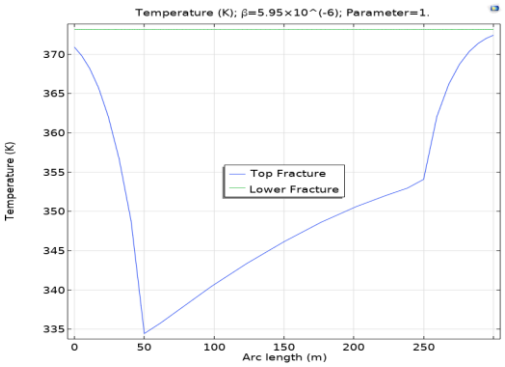

Figure 10-28. Temp: $\beta = 5.95 \times 10^{-6}$

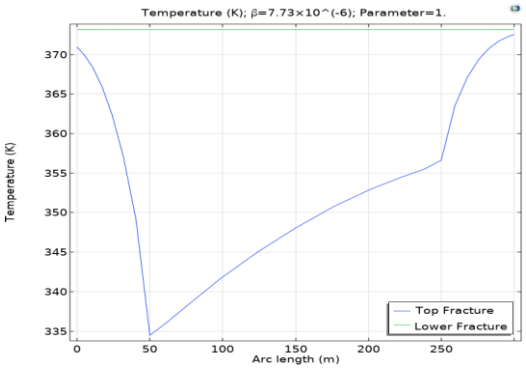

Figure 10-29 Temp: $\beta = 7.73 \times 10^{-6}$

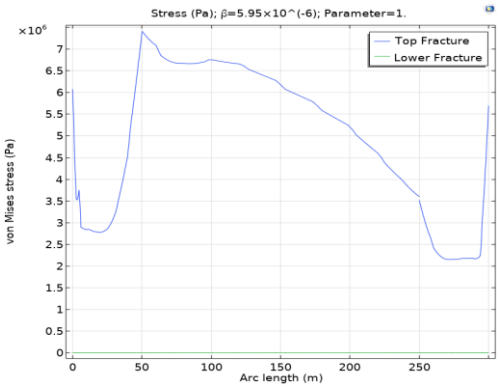

Figure 10-30 Stress for 5.95×10^{-6}

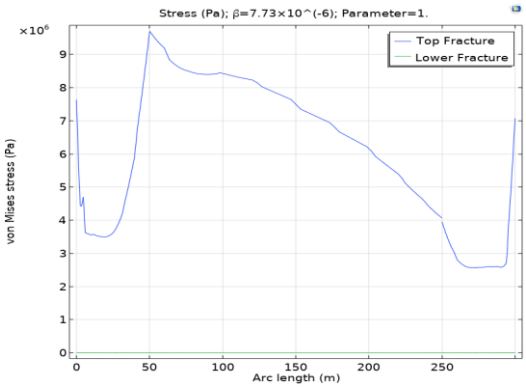

Figure 10-31 Stress for $\beta = 7.73 \times 10^{-6}$

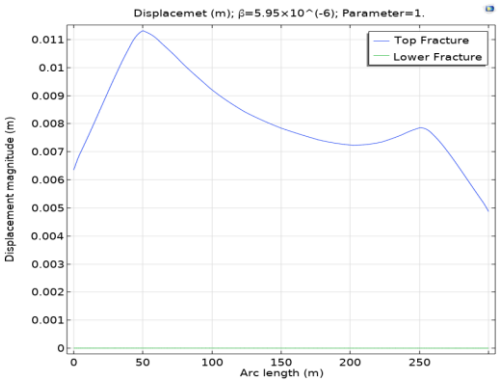

Figure 10-32 Disp. for 5.95×10^{-6}

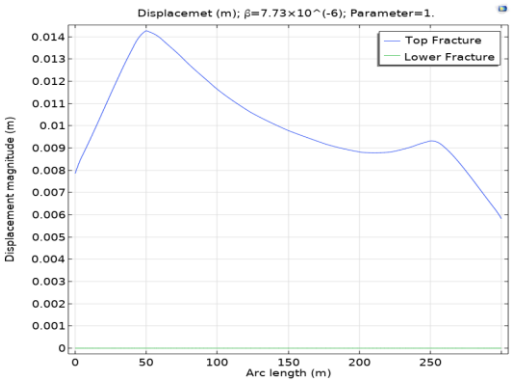

Figure 10-33 Disp. for $\beta = 7.73 \times 10^{-6}$

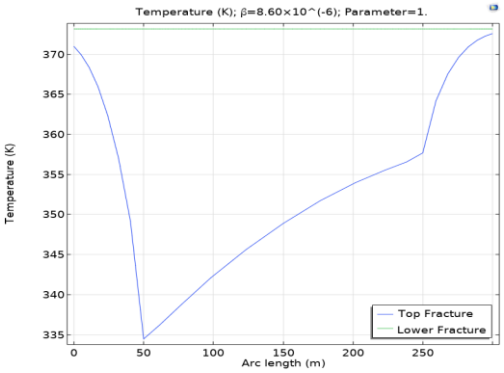

Figure 10-34 Temp: $\beta = 8.60 \times 10^{-6}$

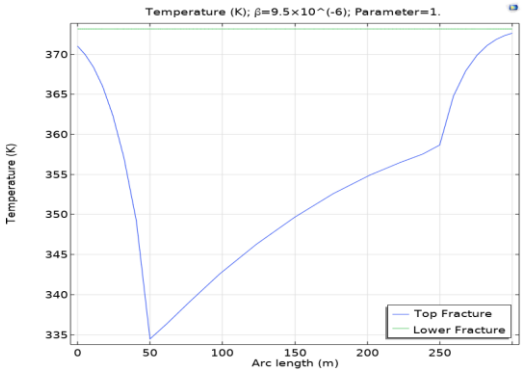

Figure 10-35 Temp for $\beta = 9.5 \times 10^{-6}$

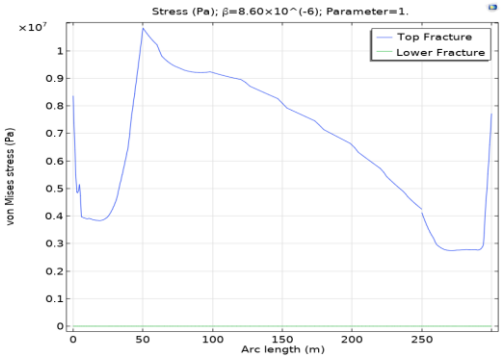

Figure 10-36 Stress: $\beta = 8.60 \times 10^{-6}$

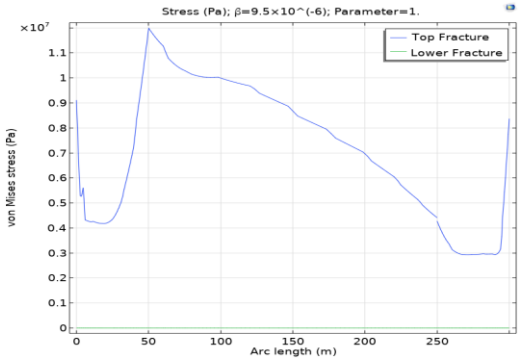

Figure 10-37 Stress: $\beta = 9.5 \times 10^{-6}$

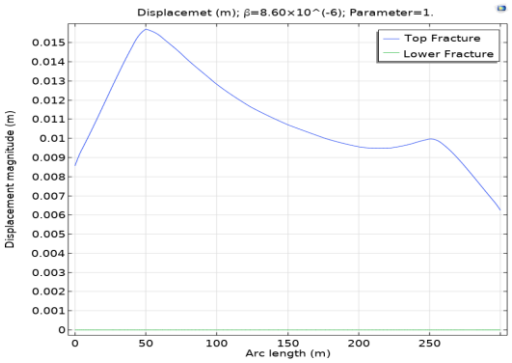

Figure 10-38 Disp. for $\beta = 8.60 \times 10^{-6}$

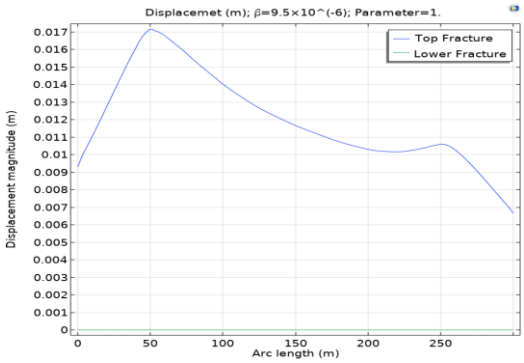

Figure 10-39 Disp. for $\beta = 9.5 \times 10^{-6}$

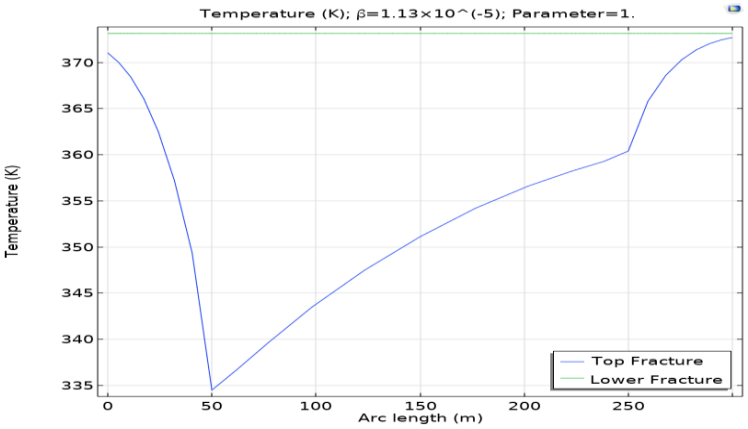

Figure 10-40 Temperature for $\beta = 1.13 \times 10^{-5}$

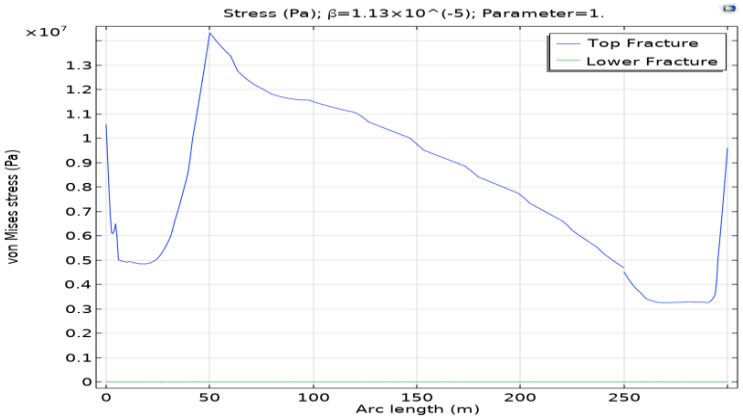

Figure 10-41 Stress for $\beta = 1.13 \times 10^{-5}$

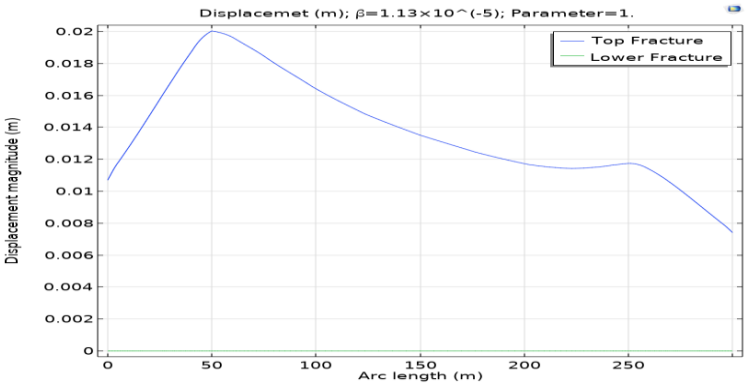

Figure 10-42 Displacement for $\beta = 1.13 \times 10^{-5}$

C. Sensitivity Analysis for Injection Rate as Mass Flux ($Inj, kg/m^2/s$)

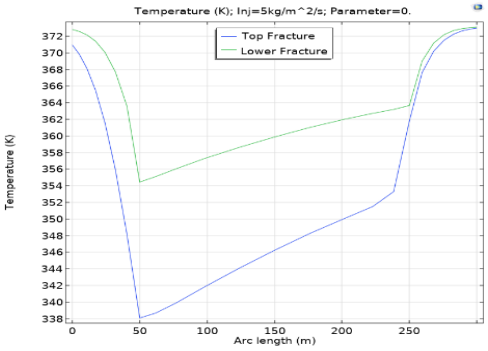

Figure 10-43 Temp for Inj= 5 $kg/m^2/s$

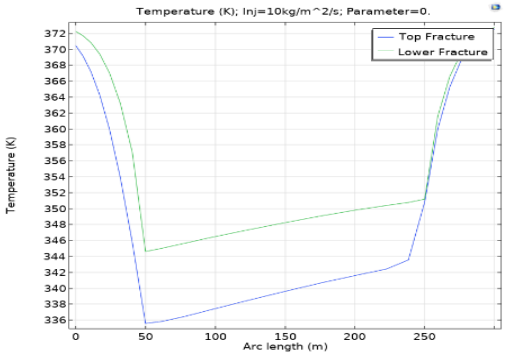

Figure 10-44 Temp for Inj= 10 $kg/m^2/s$

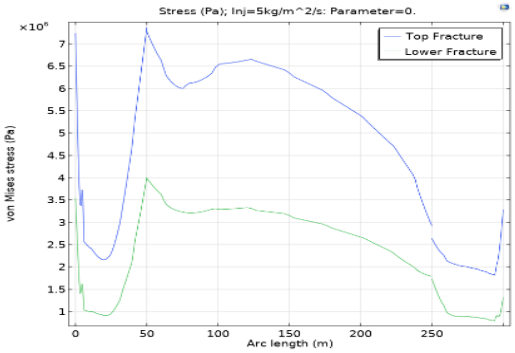

Figure 10-45 Stress for Inj= 5 $kg/m^2/s$

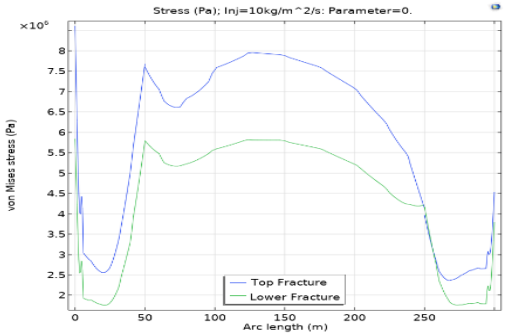

Figure 10-46 Stress for Inj= 10 $kg/m^2/s$

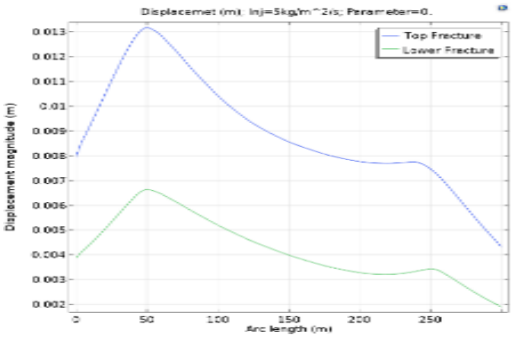

Figure 10-47 Disp. for Inj= 5 $kg/m^2/s$

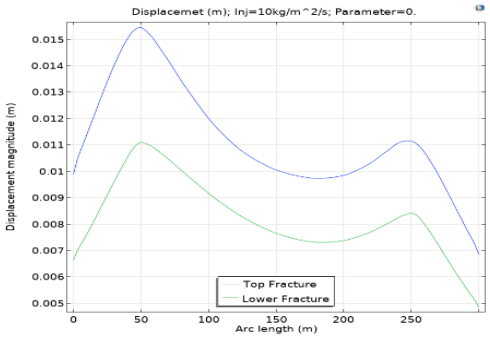

Figure 10-48 Disp. for Inj= 10 $kg/m^2/s$

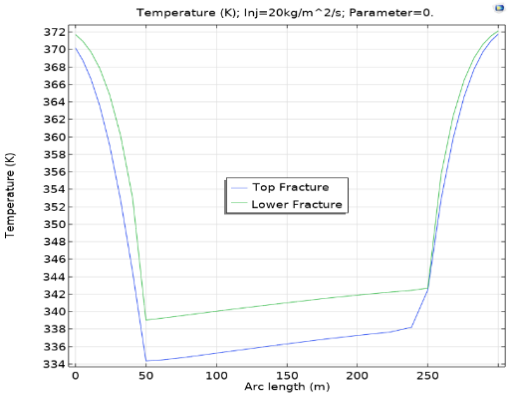

Figure 10-49 Temp: $Inj = 20\ kg/m^2/s$

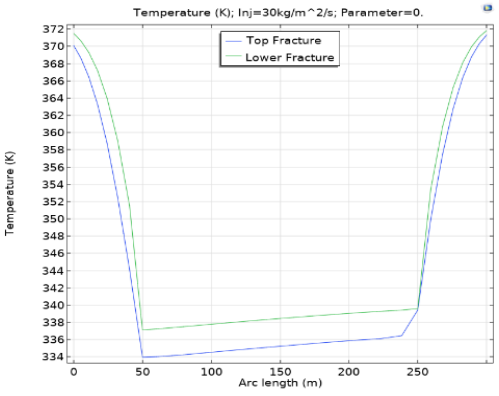

Figure 10-50 Temp: $Inj = 30\ kg/m^2/s$

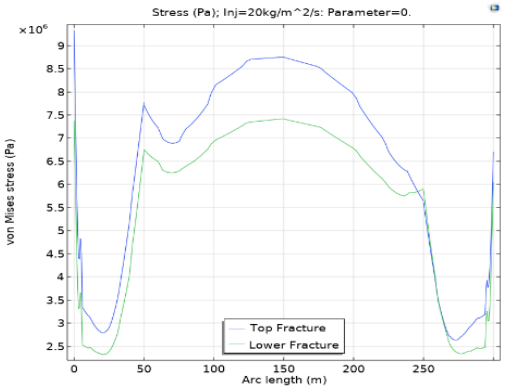

Figure 10-51 Stress: $Inj = 20\ kg/m^2/s$

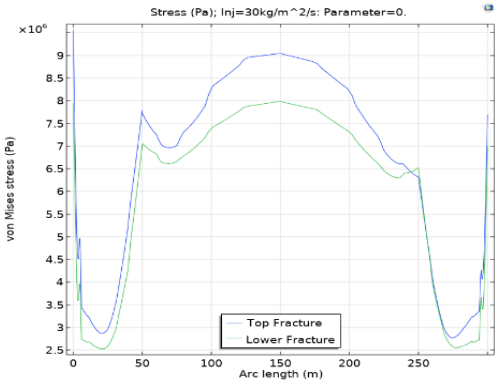

Figure 10-52 Stress: $Inj = 30\ kg/m^2/s$

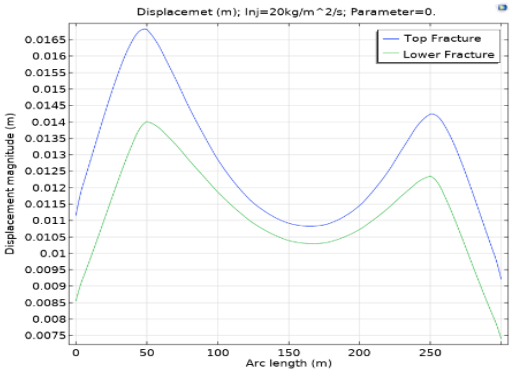

Figure 10-53 Disp: $Inj = 20\ kg/m^2/s$

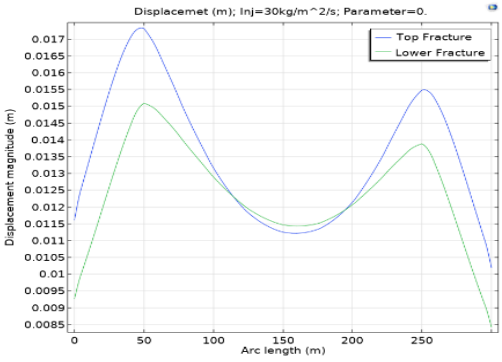

Figure 10-54 Disp: $Inj = 30\ kg/m^2/s$

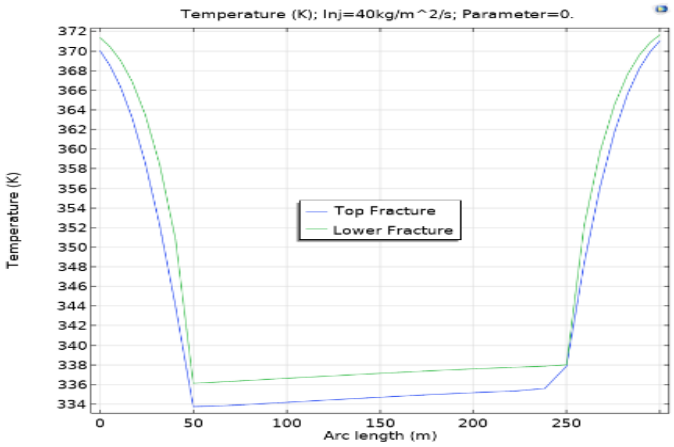

Figure 10-55 Temperature for $Inj = 40\ kg/m^2/s$

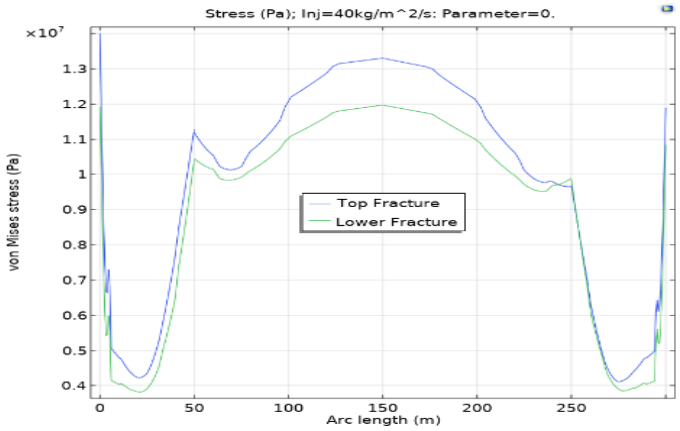

Figure 10-56 Stress for $Inj = 40\ kg/m^2/s$

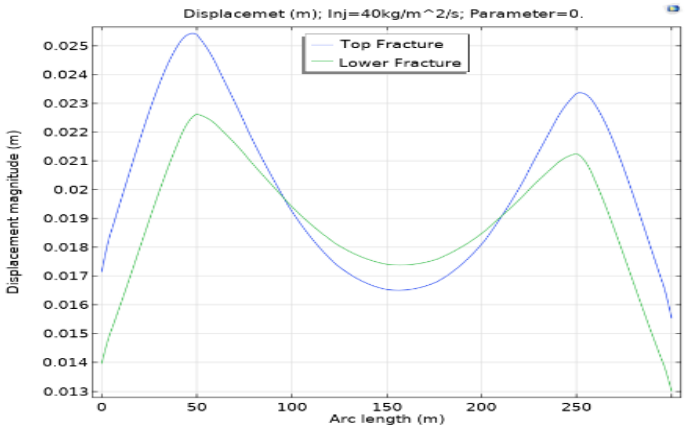

Figure 10-57 Displacement for $Inj = 40\ kg/m^2/s$

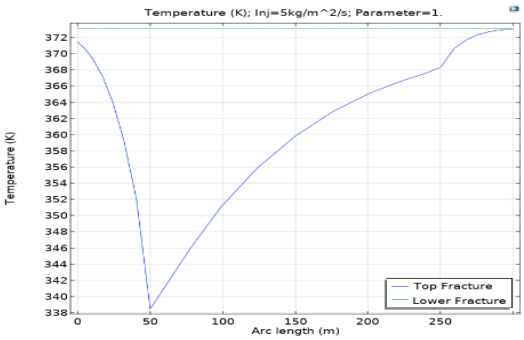

Figure 10-58 Temp for $Inj = 5\ kg/m^2/s$

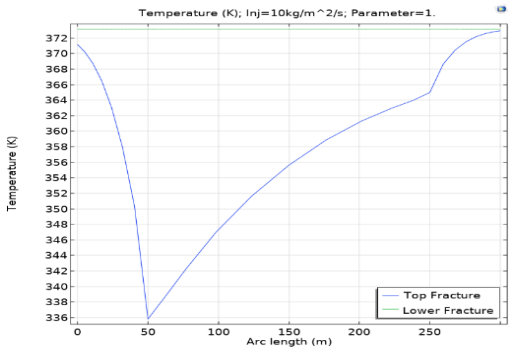

Figure 10-59 Temp: $Inj = 50\ kg/m^2/s$

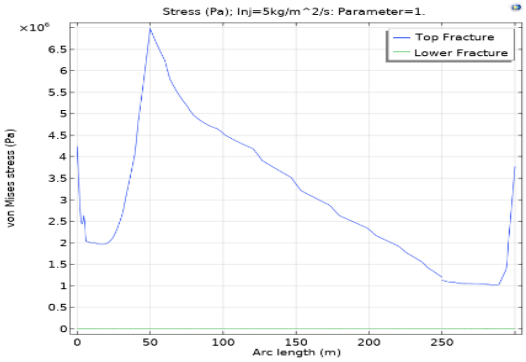

Figure 10-60 Stress for $Inj = 5\ kg/m^2/s$

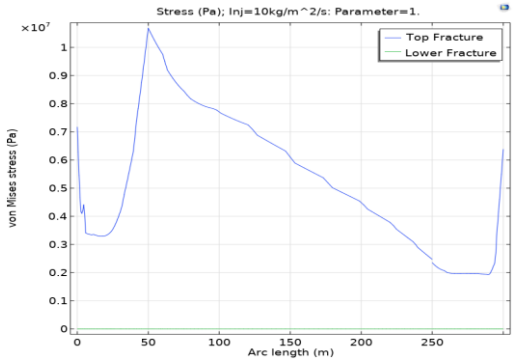

Figure 10-61 Stress: $Inj = 10\ kg/m^2/s$

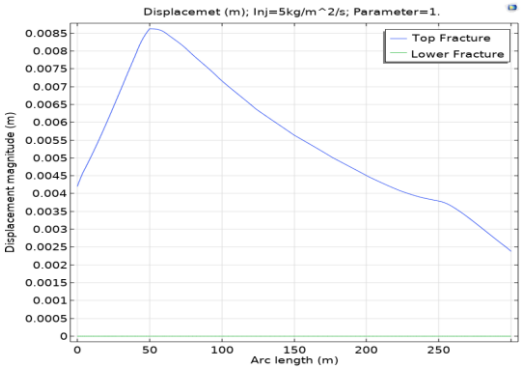

Figure 10-62 Disp. for $Inj = 5\ kg/m^2/s$

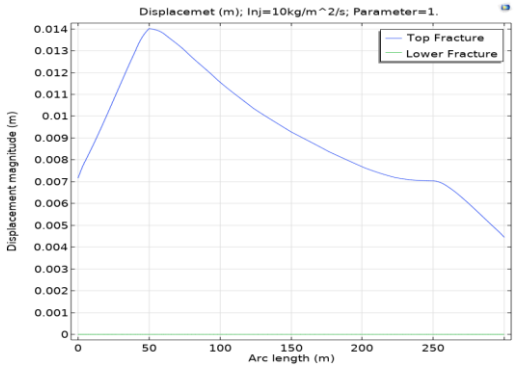

Figure 10-63 Disp. for $Inj = 10\ kg/m^2/s$

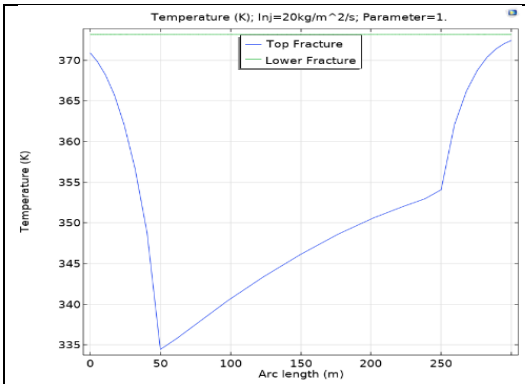

Figure 10-64 Temp: $Inj = 20\ kg/m^2/s$

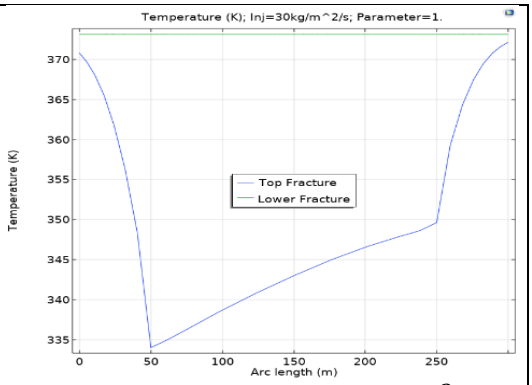

Figure 10-65 Temp: $Inj = 30\ kg/m^2/s$

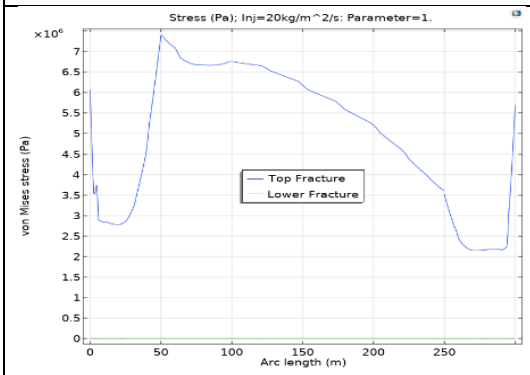

Figure 10-66 Stress: $Inj = 20\ kg/m^2/s$

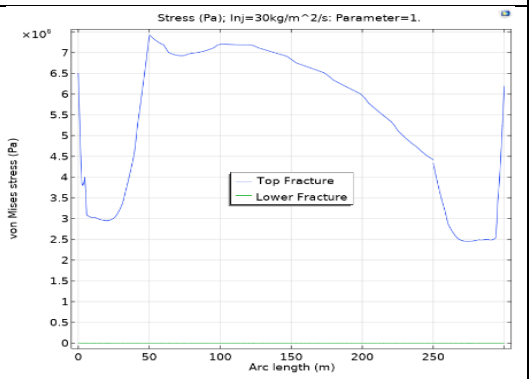

Figure 10-67 Stress: $Inj = 30\ kg/m^2/s$

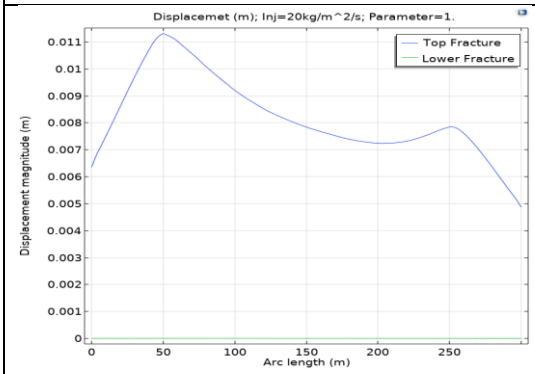

Figure 10-68 Disp: $Inj = 20\ kg/m^2/s$

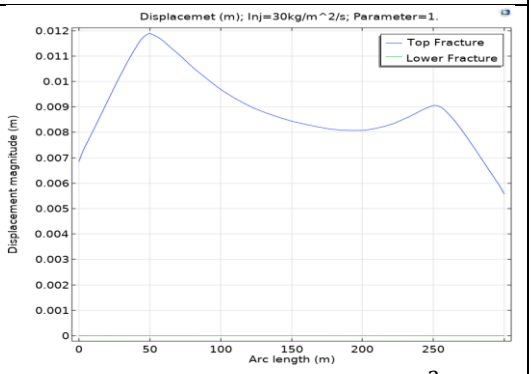

Figure 10-69 Disp: $Inj = 30\ kg/m^2/s$

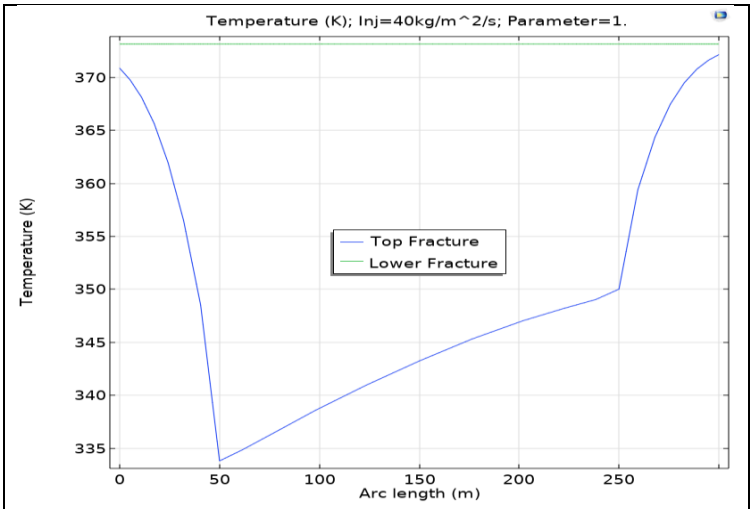

Figure 10-70 Temperature for $Inj = 40\ kg/m^2/s$

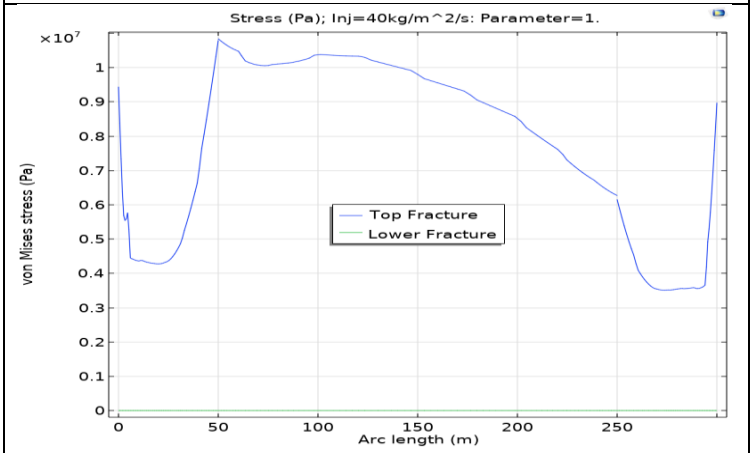

Figure 10-71 Stress for $Inj = 40\ kg/m^2/s$

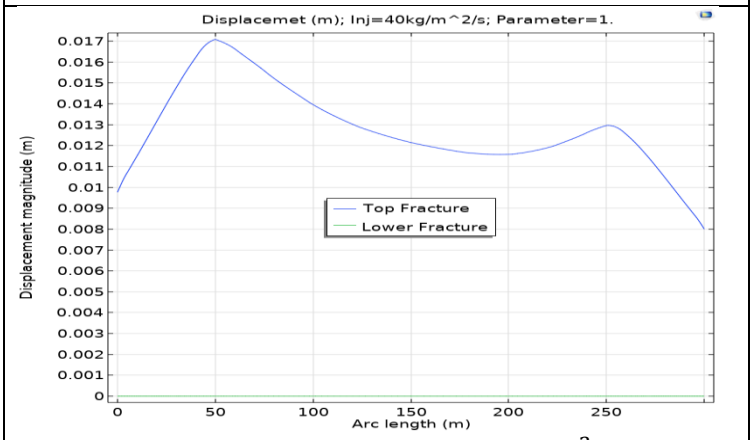

Figure 10-72 Displacement for $Inj = 40\ kg/m^2/s$

D. Boundary Pressure Oscillation: Mandel Problem Revisited

Figure 10-73 to Figure - 10-75 show the sequence of smoothening oscillations as number of elements increases; in other words, as meshing gets finer to better discretize the boundary. It is obvious that if we have a more powerful computer to further increase the number of elements, we could eventually eliminate the oscillation to obtain a perfect curve.

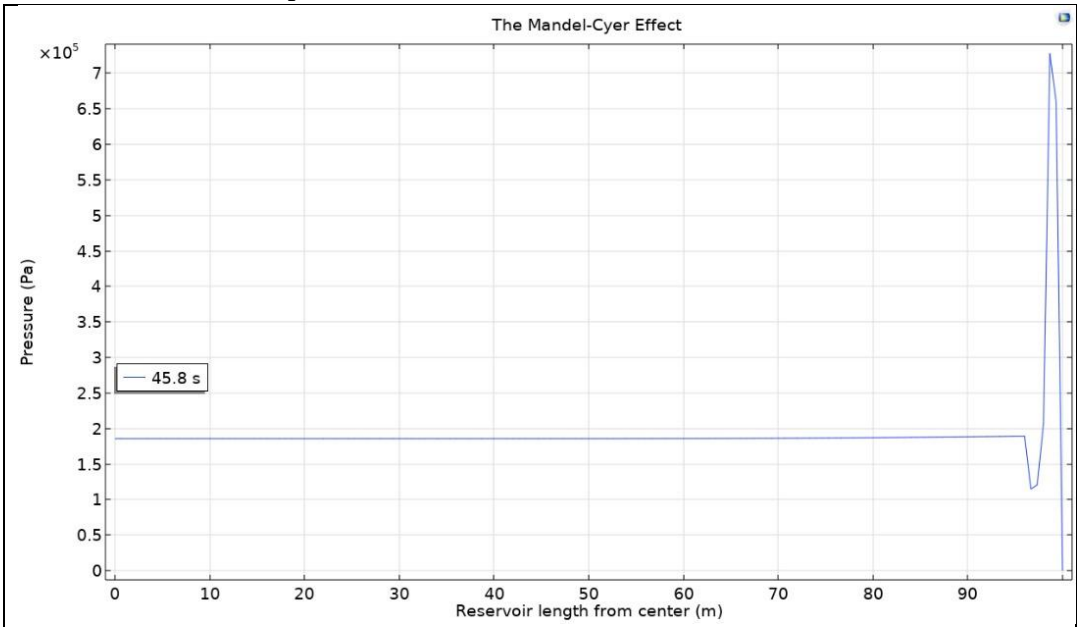

Figure 10-73. Boundary pressure when element size is 750

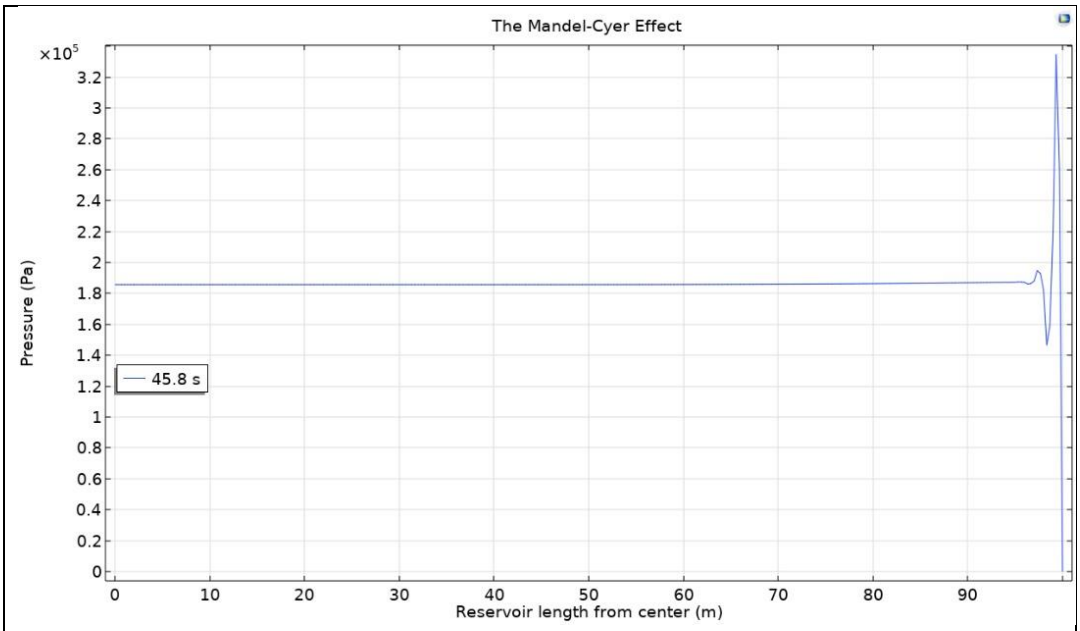

Figure - 10-74. Boundary pressure when element number is increased to 3000. Notice how oscillation decreases.

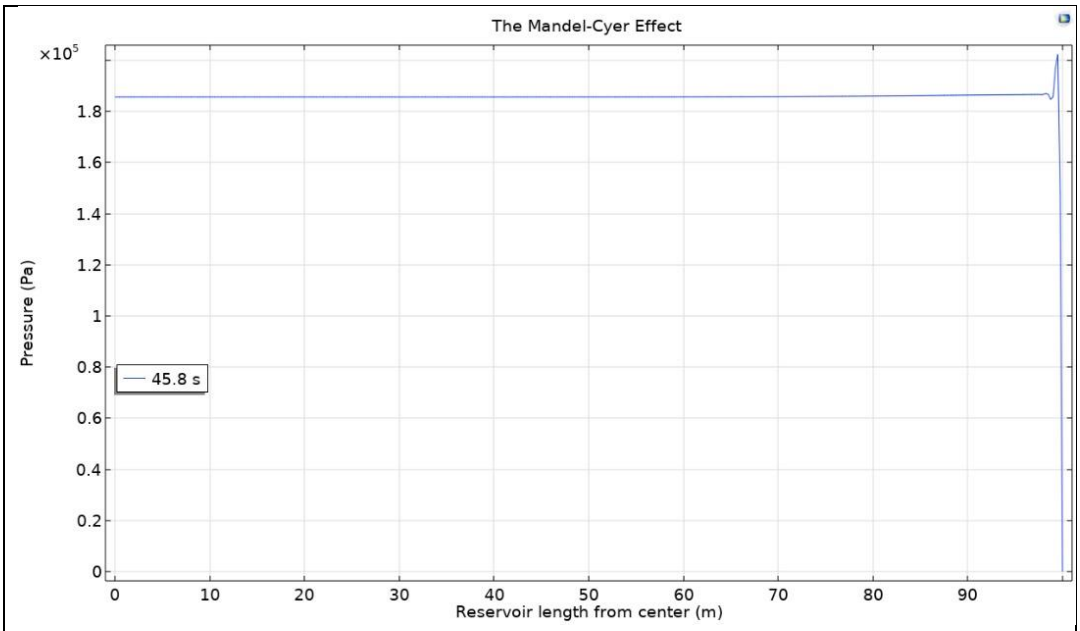

Figure - 10-75. Boundary pressure when number of elements increases to 12000. Oscillation gets even smoother.

E. Simplified 3-D EGS Model: Chronological Surface Temperature

Observe the thermal breakthrough at 3 years and the subsequent cooling of almost half of the domain by the eighth year.

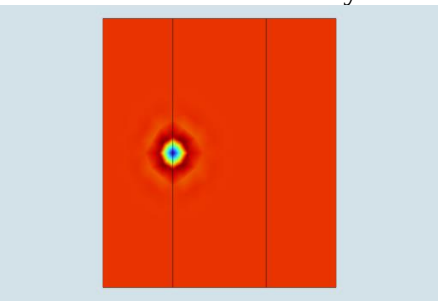

10-76. t = 0 year

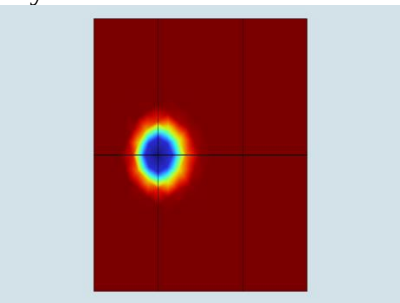

10-77. t = 0.5 year

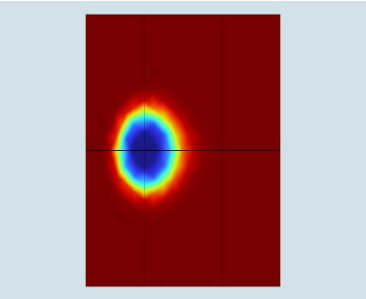

10-78. t = 1 year

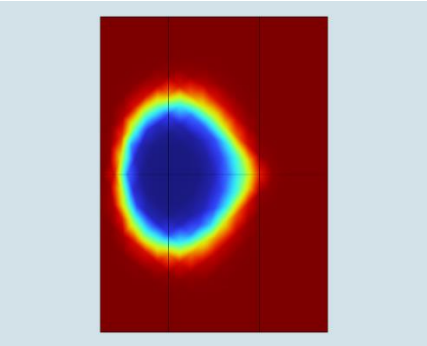

10-79. t = 3 years

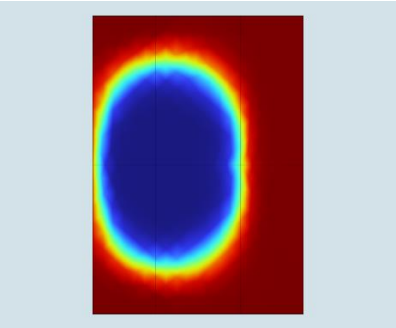

10-80. t = 8 years

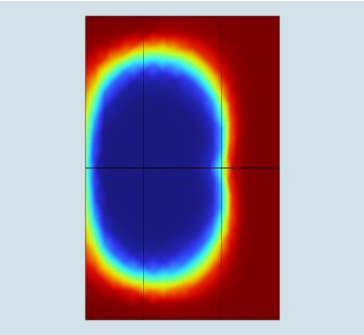

10-81. t = 10 years